

Investigation of entrance-channel barrier distribution and charged-particle emission in the $^{51}\text{V} + ^{159}\text{Tb}$ reaction

P. Brionnet^{1,*}, T. Cap², M. Forge³, T. Fukatsu⁴, H. Haba¹, D. Kaji¹, S. Kimura⁵, K. Morimoto¹, Y. Michimoto⁴, T. Niwase⁴, M. Tanaka⁶, S. Sakaguchi⁴, H. Sakai¹ and Y. Yamanouchi⁴

¹*RIKEN Nishina Center, 2-1 Hirosawa, Wako, Saitama 351-0106, Japan*

²*National Centre for Nuclear Research, Pasteura 7, 02-093 Warsaw, Poland*

³*Université de Strasbourg, CNRS, IPHC UMR 7178, F-67000 Strasbourg, France*

⁴*Department of Physics, Kyushu University, 744, Motoooka, Nishi-ku, Fukuoka 819-0395, Japan*

⁵*KEK Wako Nuclear Science Center, Wako, Saitama 351-0106, Japan*

⁶*Faculty of Arts and Science, Kyushu University, 744, Motoooka, Nishi-ku, Fukuoka 819-0395, Japan*



(Received 19 August 2024; revised 18 October 2024; accepted 7 November 2024; published 2 December 2024)

This study investigates the $^{51}\text{V} + ^{159}\text{Tb} \rightarrow ^{210}\text{Ra}^*$ reaction through measurements of both the entrance-channel barrier distribution and detailed excitation functions for the xn , pxn , and αxn channels over a wide energy range. This research extends systematic studies of reactions involving beams heavier than ^{48}Ca on deformed heavy targets, linking cross section measurements to the side-collision configuration effects observed in superheavy nuclei synthesis. Additionally, a significant enhancement of channels with charged-particle emission is observed compared to the neutron exit channels, with the $\alpha 3n$ channel yielding a peak cross section of $41.7 \pm 5.0 \mu\text{b}$ at $E_{\text{c.m.}} = 177.7 \pm 1.5 \text{ MeV}$, an order of magnitude higher than $4.7 \pm 1.5 \mu\text{b}$ measured at the peak of the $3n$ exit channel at $E_{\text{c.m.}} = 162.5 \pm 1.5 \text{ MeV}$. Comparisons with reactions using the same target but different projectiles, ^{48}Ca and ^{50}Ti , which do not exhibit such enhancement, are discussed. The analysis, interpretation, and comparison with theoretical calculations are performed using the CCFULL code and a statistical model.

DOI: [10.1103/PhysRevC.110.064601](https://doi.org/10.1103/PhysRevC.110.064601)

I. INTRODUCTION

With the synthesis and official recognition of the superheavy elements (SHEs) $Z = 113$, 115 , 117 , and 118 in 2016, the seventh row of the periodic table was completed [1]. These discoveries and studies at the very end of the nuclear chart provide essential information regarding the predicted island of enhanced stability of superheavy nuclei, expected to be around $Z = 114$ or 120 and $N = 184$ [2]. They can also deliver crucial information regarding the limits of nuclear existence in this extreme mass region.

All elements beyond nihonium ($Z = 113$) were synthesized using hot-fusion reactions based on actinide targets and the doubly magic ^{48}Ca beam [3]. Oganesson ($Z = 118$) is the final element accessible using this projectile, as no heavier target material than californium is available in sufficient amounts [4]. Therefore, the search for new elements must involve beams heavier than ^{48}Ca , with either ^{50}Ti , ^{51}V , or ^{54}Cr on deformed actinide targets. Some attempts have already been made using these heavier beams, but none have been successful in producing new elements or isotopes so far, and only upper limit cross sections have been reported [5–7].

However, recent reports of the successful production of ^{290}Lv [8] in the reaction of ^{50}Ti with a ^{244}Pu target show that superheavy nuclei can also be produced in reactions with

projectiles heavier than ^{48}Ca . Up to now, in the heavy and superheavy mass region, heavier beams have only been successfully used with ^{208}Pb or ^{209}Bi [9–13] spherical targets. New experimental data involving heavier beams on actinide targets are important for tuning theoretical models to provide reliable predictions for new reactions. Cross sections and optimal beam energies for the synthesis of new elements are currently extrapolated from ^{48}Ca -induced reactions, as very little information is available on reactions involving deformed actinide targets with heavier beams.

The systematic study of reactions using ^{50}Ti , ^{51}V , or ^{54}Cr beams on actinide targets is crucial. It can provide valuable information for the success of current and future searches for new elements and can be used to test available reaction models and improve their predictive powers in the SHE mass region. Unfortunately, a systematic study of fusion-evaporation reactions using ^{50}Ti , ^{51}V , or ^{54}Cr beams on actinide targets is difficult due to the very low cross sections, estimated to be at the femtobarn level. However, some valuable information might be obtained by studying reactions with lighter targets such as lanthanides.

In this paper, we present a study of the reaction of a ^{51}V projectile with the deformed ^{159}Tb target. The use of a deformed lanthanide target might serve as an analog for the ^{248}Cm target currently used in the search for the new element with $Z = 119$ at RIKEN [14] using a ^{51}V projectile. The lighter ^{159}Tb has deformation parameters similar to those of ^{248}Cm ($\beta_2 = 0.271$, $\beta_4 = 0.066$ for ^{159}Tb compared with

*Contact author: pierre.brionnet@riken.jp

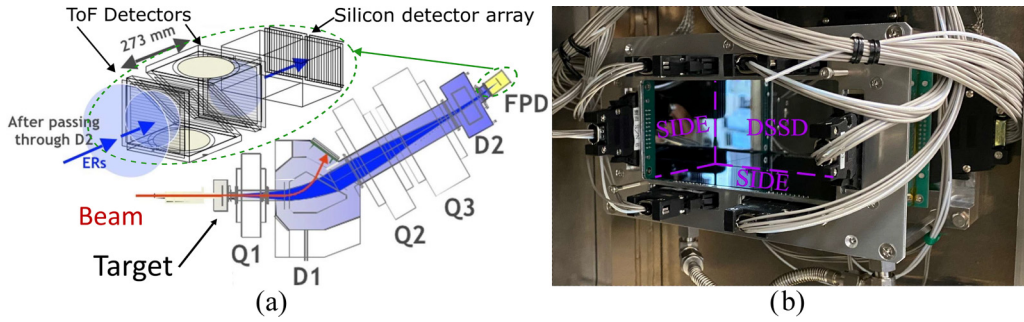


FIG. 1. (a) Visualization of the GARIS-III separator and its optical configuration [22]. The detector system (top left) is positioned at the focal plane of the separator and is composed of two time-of-flight detectors and a silicon detector array (see text for detailed information). (b) Photograph of the silicon detector array used for the detection of the nuclei of interest at the focal plane of the separator mounted inside the vacuum chamber.

$\beta_2 = 0.286$, $\beta_4 = 0.039$ for ^{248}Cm). Additionally, the evaporation residue production rates for ^{159}Tb are significantly higher, in the μb range, allowing a detailed study of the reaction mechanisms and evaporation process. Additionally, comparing the $^{51}\text{V} + ^{159}\text{Tb}$ reaction with the results of ^{48}Ca and ^{50}Ti reactions with the same target might provide insights into how the fusion probability changes with different projectile nuclei. However, the comparison of these systems with the actinide targets stops here, as the other characteristics and properties such as mass asymmetry, fusion hindrance, and properties of the compound nuclei, differ considerably (fission barrier, nuclear deformation map, etc.).

This study investigates the effect of the incident beam energy and the impact of the nuclear deformation on the optimal beam energy for the $^{51}\text{V} + ^{159}\text{Tb}$ reaction. In this study, both the barrier distribution and the detailed excitation function for various exit channels (e.g., xn , pxn , αxn , ...) have been measured. The objective of this study is to extend the systematic investigation of the quasielastic (QE) barrier distribution and to explore the side-collision configuration effect observed with actinide targets in previous research on hot fusion reactions in the SHE region [15–17]. In the case of prolate-deformed actinide targets, the optimum beam energy for the xn channels was observed to be higher than the average entrance-channel barrier height. This phenomenon contrasts with cold-fusion reactions on the spherical ^{208}Pb and ^{209}Bi targets in which the optimal beam energy is located around the average entrance-channel barrier height [18].

An understanding of this difference in behavior is crucial for the selection of the optimal beam energy when searching for new elements. The higher reported optimal beam energies for reactions with actinide targets correspond to a side-collision configuration rather than a tip-to-tip collision configuration, as reported in [16,17]. However, these observations were only obtained using a ^{48}Ca beam and never tested or confirmed with heavier beams. In this study, we investigate whether the side-collision effect observed in the SHE region [16] can also be observed using the lighter deformed ^{159}Tb target. Such effects are predicted by coupled-channel calculations [19].

Moreover, previous studies [15,16] have highlighted the fact that the relation between the QE barrier distribution and

the maximum cross section is also directly related to the reaction dynamics. Thus, measurements of the barrier distribution and detailed excitation functions can help us to better understand the reaction mechanism.

II. EXPERIMENTAL SETUP

The ^{51}V beam was delivered by the newly upgraded Superconducting RIKEN Linear Accelerator (SRILAC) [14]. The $^{51}\text{V}^{13+}$ ions were extracted from the 28 GHz superconducting ECR ion source and subsequently injected into SRILAC. The energy was tuned to the desired value and the beam transported to the target position of the GARIS-III separator [14,20] [see Fig. 1(a)].

The beam energy was determined and monitored by measuring the magnetic rigidity in a 90° -bending dipole magnet at the end of SRILAC in addition to an in-beam time-of-flight (TOF) measurement. These measurements provided a typical accuracy of less than 0.1%, not considering systematic uncertainties. The barrier distribution measurements were performed with beam energies ranging from 196 to 260 MeV in 2 MeV steps, corresponding to mid-target energies in the center-of-mass frame between 129.4 and 179.3 MeV. In the case of the excitation functions measurements, the beam energies ranged from 229.3 to 272.1 MeV, corresponding to mid-target energies in the center-of-mass frame between 155 and 189.2 MeV, with 3.8 MeV steps.

The barrier distribution measurements used a fixed ^{159}Tb target and a beam intensity of 1.54 p nA, or $\approx 9 \times 10^8$ particles per second. The excitation functions measurements were performed using 16 ^{159}Tb targets mounted on a rotating wheel, with beam intensities ranging from 152 to 345 p nA, depending on the beam energy.

The targets were composed of metallic ^{159}Tb sputtered onto a $2.83 \pm 0.07 \mu\text{m}$ titanium backing. The target thickness for the barrier distribution measurement was $293 \pm 10 \mu\text{g cm}^{-2}$. The measured average target thickness of the 16 sectors for the excitation function measurement was $364 \pm 16 \mu\text{g cm}^{-2}$.

The transport of nuclei of interest, such as targetlike nuclei produced in QE backscattering at 0° or evaporation residues (ER), as well as the rejection of background events, was

handled by the GARIS-III separator [14,20] shown in Fig. 1(a). The separator was filled with helium gas, at 0.9 Torr for the barrier distribution measurements and 0.55 Torr for the excitation function measurements. The vacuum in the upstream beam line was maintained by a differential pumping system [14,20] located before the target chamber. The detector chamber located at the focal plane of GARIS-III was isolated using a 0.5 μm Mylar foil to ensure the high-vacuum conditions required for the operation of the TOF detectors. The magnetic rigidity ($B\rho$) of GARIS-III was carefully selected and tuned to keep the transmission of the events of interest at the focal plane at its highest throughout the experiment. Furthermore, the newly upgraded beam stop of GARIS-III [21] was used in the barrier distribution measurements. Thanks to its design, a strong reduction of the beamlike nuclei at the focal plane of the separator was obtained, rendering the identification of the targetlike nuclei at the focal plane position possible. The beam stop was set at a fixed position of 13 cm from its reference point throughout the data acquisition to ensure reliable and stable conditions.

The focal plane detector array of GARIS-III consists of two sets of detectors (Fig. 1). First, two high-performance TOF detectors are positioned upstream of the focal plane of the separator [23] for the detection of the incoming ions exiting GARIS-III. These detectors are used to identify the different reaction products transported and implanted in the silicon detectors based on their masses. Each TOF detector is composed of a 120-mm-diameter window of 0.5- μm -thick Mylar foil with a 19.3 $\mu\text{g cm}^{-2}$ gold deposit, an electrostatic deflector, and a microchannel plate (120-D-40:1-NR PHOTONIS) [23]. The detectors are spaced 273 mm apart, with the rear TOF detector located 137 mm upstream of the focal plane and the silicon array.

The silicon detector array consists of six silicon detectors newly developed by Hamamatsu and is positioned at the focal plane of the GARIS-III separator [Fig. 1(b)]. One 300- μm -thick double-sided silicon-strip detector (DSSD) of $12.3 \times 6 \text{ cm}^2$, 64×64 strips ($2 \times 1 \text{ mm}^2$ pixel size), is placed along the momentum dispersive direction of the separator (X axis). This DSSD is used for the detection of all incoming ions exiting the separator, as well as the detection of their subsequent decay, and is surrounded by four 320- μm -thick silicon pad detectors (two $6 \times 6 \text{ cm}^2$, 4×4 pads, and two $12.3 \times 6 \text{ cm}^2$, 4×8 pads) mounted upstream in a box geometry (Fig. 1(b)). This allows for the efficient detection of ions and charged particles emitted during the subsequent decays of the implanted nuclei that escape the DSSD. Finally, one 650- μm -thick silicon 4×8 pad detector, $12.3 \times 6 \text{ cm}^2$, is placed directly behind the implantation detector. This detector is used as a veto for the suppression of light charged particles crossing the DSSD, the primary source of background events in the α -decay spectrum, as described and studied by Brionnet *et al.* [24].

Measurement of the dose and monitoring of the beam intensity were performed by detecting the Rutherford-scattered ^{51}V nuclei at the target position. The measurement was performed at $\theta_{\text{lab}} = 45^\circ$ using a silicon detector (S1223-01 Hamamatsu) at 186 mm from the target with a 2.5-mm-diameter collimator.

III. BARRIER DISTRIBUTION

A. Experimental method

The QE barrier distribution of the $^{51}\text{V} + ^{159}\text{Tb}$ system was measured similarly to the method used by Tanaka *et al.* [15] by detecting the QE backscattering of targetlike nuclei. GARIS-III was used to measure the scattering of the recoiled targetlike nuclei at 0° , which corresponds to the backscattering of the projectilelike nuclei at 180° . The barrier distribution $D(E_{\text{c.m.}})$, as a function of the center-of-mass energy, was obtained using the following equation:

$$D(E_{\text{c.m.}}) = -\frac{dR}{dE_{\text{c.m.}}} \equiv -\frac{d}{dE_{\text{c.m.}}} \left(\frac{d\sigma_{\text{QE}}}{d\sigma_{\text{Ruth}}} \right), \quad (1)$$

where $R(E_{\text{c.m.}}) \equiv \frac{d\sigma_{\text{QE}}}{d\sigma_{\text{Ruth}}}$ is the reflection probability and corresponds to the ratio of the QE backscattering cross section to the Rutherford scattering cross section at a fixed angle at the target position. Here, $R(E_{\text{c.m.}})$ can be extracted experimentally through the direct ratio between the number of detected elastically scattered ^{51}V ions at the target position, $N_{\text{Ruth}}[^{51}\text{V}]$, to the number of recoiled QE backscattered ^{159}Tb -like nuclei at $\theta_{\text{lab}} = 0^\circ$ measured by the focal plane detector array, $N_{\text{QE}}[^{159}\text{Tb}]$, using the following expression:

$$R(E_{\text{c.m.}}) \equiv C \times \frac{N_{\text{QE}}[^{159}\text{Tb}]}{N_{\text{Ruth}}[^{51}\text{V}]}, \quad (2)$$

where C is the normalization coefficient of the reflection probability. It also includes corrections and adjustments required to compensate for experimental conditions.

B. Experimental data analysis

Identification of the QE backscattering nuclei at the focal plane was performed using the TOF- E_{DSSD} matrix, combining the TOF information and DSSD signals. Figure 2 presents the energy in the DSSD as a function of the TOF of the ions exiting the separator at three beam energies: $E_{\text{c.m.}} = 129.38$, 153.37, and 171.33 MeV.

Based on the geometry of the detection system, the kinematical correlation curve between the TOF and the energy in the DSSD for mass number $A = 159$ (targetlike nuclei) can be estimated, as shown by the red dashed line in Fig. 2. Figure 2 also illustrates that the target-like nuclei are well separated from the different types of background events transported to the focal plane. Using the same kinematical correlation curve, the primary background components in Fig. 2 can be identified by mass. These are projectilelike nuclei and reaction products with mass numbers around $A \approx 100$, produced by the reaction of the beam ions with the titanium backing of the target.

The number of QE backscattering events corresponds to the number of targetlike nuclei identified in Fig. 2. A slightly wider gate (solid orange line in Fig. 2) was applied to the experimental signal to consider the actual characteristics and response time of the detector. Nevertheless, more than $\approx 95\%$ of the overall statistics are located in the main peak within the defined region of interest.

Even with the large acceptance of GARIS-III [20], not all the targetlike nuclei from the QE scattering are transported to

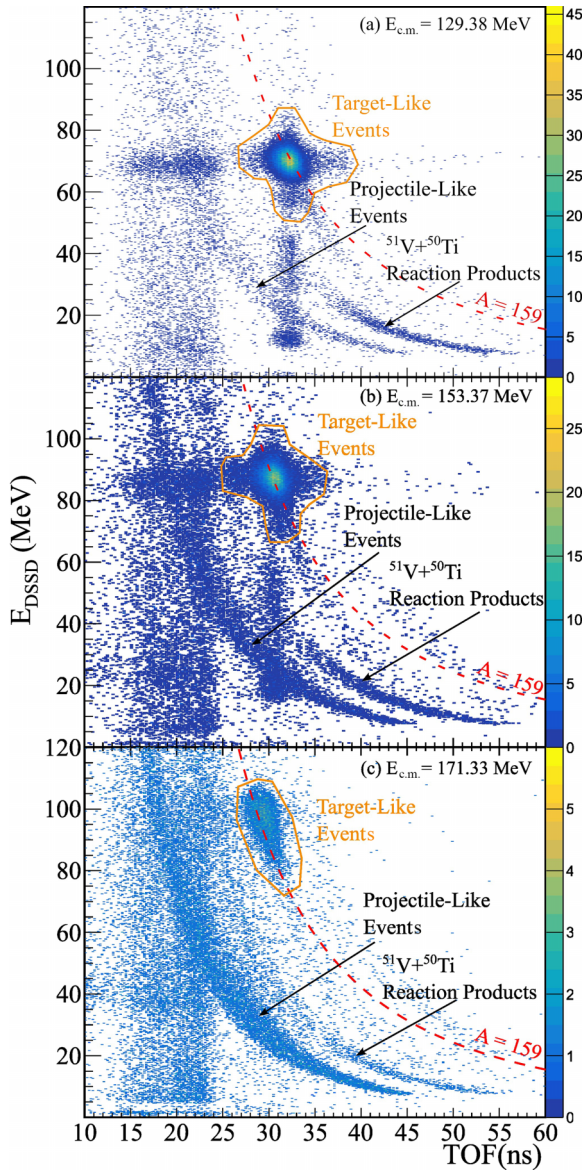


FIG. 2. Energy measured by the DSSD in MeV as a function of the TOF in ns, used for particle identification, at three beam energies: (a) $E_{c.m.} = 129.38$ MeV, (b) $E_{c.m.} = 153.37$ MeV, and (c) $E_{c.m.} = 171.33$ MeV. The solid orange line represents the selection of targetlike nuclei and the dashed red line is the correlation function for targetlike nuclei of mass number $A = 159$.

the focal plane. Thus, the transmission of the nuclei of interest needs to be closely monitored. This monitoring is performed using the characteristics of the implantation profile for the QE backscattering in the DSSD throughout the measurement to ensure stable and reliable conditions.

The dispersive axis of the separator (along the X axis of the DSSD) is the most susceptible to these transmission changes. The x -position distribution width of QE backscattered events is comparable to the acceptance of the TOF and the size of the DSSD detector, as presented in Fig. 3.

The measured full width at half maximum (FWHM) of the distribution was approximately 76.5 strips, or about 153 mm,

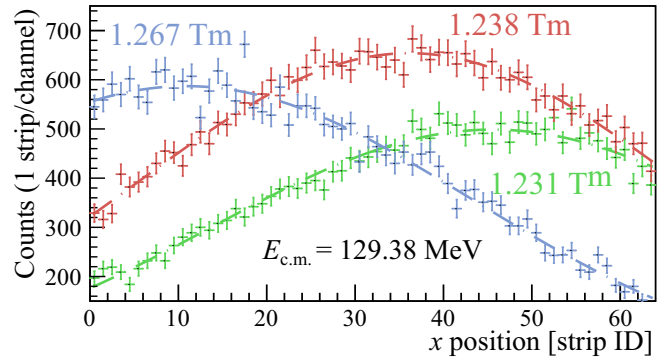


FIG. 3. Evolution of the implantation profile for three magnetic rigidities at $E_{c.m.} = 129.38$ MeV: 1.267 T m in blue, 1.238 T m in red, and 1.231 T m in green. The dashed lines represents the Gaussian fits of the profiles, from which the values of x_{center} are extracted.

for the $^{51}\text{V} + ^{159}\text{Tb}$ system. Therefore, even a small shift in the distribution of the center position (x_{center}) could significantly affect the transmission and needs to be closely monitored and corrected.

Transmission monitoring throughout the experiment was performed by measuring the dependence between the x -position distribution and the relative transmission of the events of interest. This dependence was measured at five energies ($E_{c.m.} = 129.38, 151.39, 163.37, 169.35,$ and 176.34 MeV), by scanning the magnetic rigidity of GARIS-III while measuring the mean value of the x -position distribution, x_{center} , and the number of QE scattering events.

Figure 3 presents the evolution of the x position distribution at three magnetic rigidities at the same energy $E_{c.m.} = 129.38$ MeV. The value of x_{center} was extracted using a Gaussian fit, as shown in Fig. 3 by the colored dashed lines.

Figure 4 presents the correlation between the relative transmission and the value of x_{center} measured at five beam energies. The magnetic rigidity of GARIS-III was adjusted throughout the experiment to maintain the relative transmission above 95%, by maintaining x_{center} in the region highlighted in yellow in Fig. 4: between strips 15 and 38.

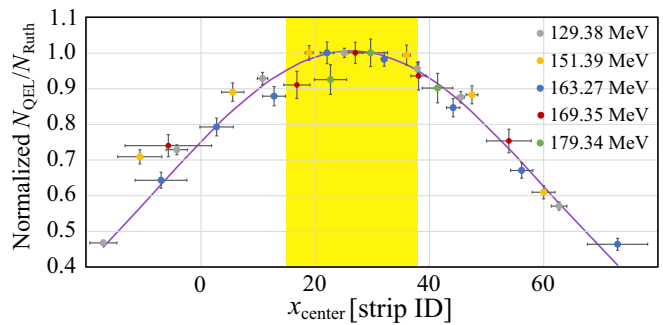


FIG. 4. Normalized relative transmission efficiency as a function of the center (x_{center}) of the implantation distribution for five beam energies. The solid purple line denotes a Gaussian function fitted to the data to define the optimal region of measurement. This region of interest is highlighted in yellow and corresponds to relative transmissions $\geq 95\%$.

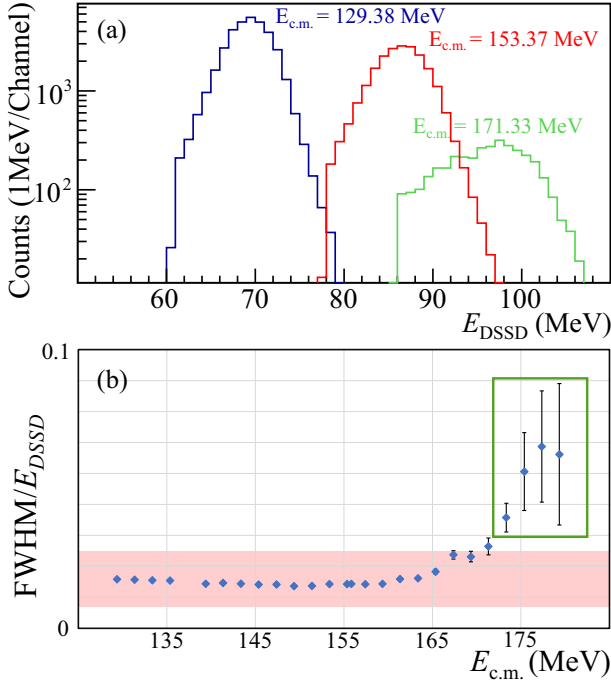


FIG. 5. (a) Implantation-energy spectrum on a logarithmic scale of the targetlike nuclei at three energies: $E_{c.m.} = 129.38, 153.37$ and 171.33 MeV in blue, red, and green, respectively. (b) Evolution of the FWHM of the implantation-energy distribution of the targetlike nuclei as a function of the center-of-mass frame energy. The highlighted region represents the standard deviation of the data, excluding the last three points, where contamination from deep-inelastic events was too high. Due to this, the points within the green square were treated as upper limits in the analysis.

Furthermore, to reduce the uncertainties in the measurement of $N_{QE}[^{159}\text{Tb}]$, the relative transmission for distributions with $15 \leq x_{\text{center}} \leq 38$ was corrected using a Gaussian fit to the data (purple line in Fig. 4). From this correction, the standard deviation of the data from the fit was extracted (approximately 4% for $15 \leq x_{\text{center}} \leq 38$), and was used as a systematic error in the analysis of the barrier distribution.

The distribution along the nondispersive axis (Y axis) is well within the DSSD and TOF detector acceptance, with a FWHM of 24.75 strips (or mm). This distribution does not need close monitoring or correction, as more than 99% of the events are within the DSSD at all times.

At energies higher than the entrance-channel barrier, deep-inelastic scattering starts to occur in addition to QE scattering. This effect has also been observed in previous studies [15,16], and is detected through a broadening of the implantation-energy distribution. Figure 5(a) presents such a broadening, with the evolution of the implantation spectrum for three energies: $E_{c.m.} = 129.38, 153.37$ and 171.33 MeV in blue, red, and green, respectively. Figure 5(b) plots the measured FWHM of the energy spectrum throughout the QE barrier measurement. The evolution of this FWHM was used to track the deep-inelastic contamination. Due to probable non-negligible contamination by background events, the measurements

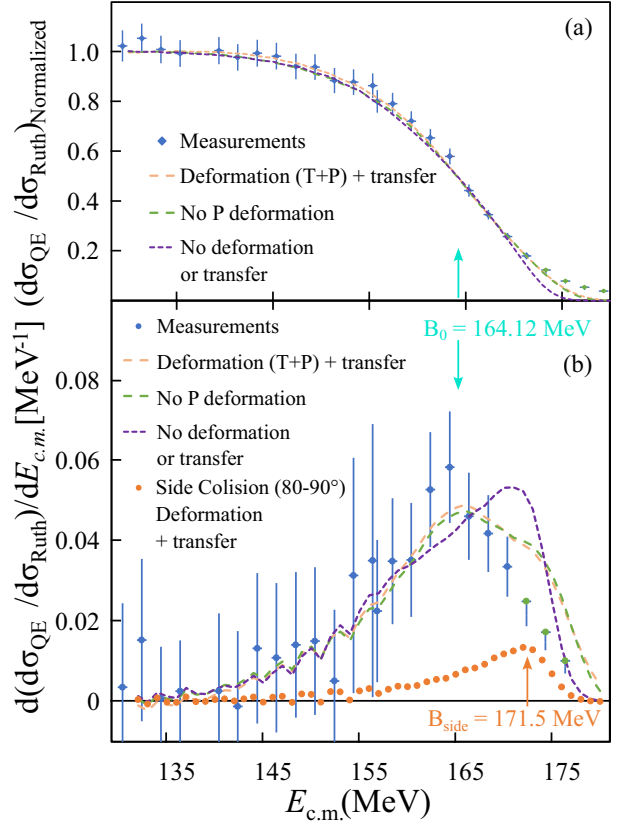


FIG. 6. Measured reflection probability $R(E_{c.m.})$ (a) and the QE barrier distribution $D(E_{c.m.})$ (b) compared to CCFULL calculations [19] based on different assumptions: the dashed orange lines represent the full coupling optimized as described in Table I, the dashed green line excludes the projectile coupling (quadrupole vibrational coupling), and the purple dashed line is without both quadrupole vibrational coupling (target and projectile) and no neutron transfer. The dotted orange distribution in the lower panel represents the side-collision component extracted from the CCFULL calculation [19] (collision angle from 80° to 90°).

performed for $E_{c.m.} \geq 173.34$ MeV (green points in later figures) are treated as upper limits only in the analysis.

C. Experimental barrier distribution

First, by the reflection probability was deduced from the ratio of the number of QE backscattering events, $N_{QE}[^{159}\text{Tb}]$, to the number of Rutherford-scattered events at the target position, $N_{Ruth}[^{51}\text{V}]$ using Eq. (2). The constant C representing the normalization factor was determined experimentally as the average of the $R(E_{c.m.})$ in the plateau region for $E_{c.m.} \leq 145.36$ MeV. Figure 6(a) shows the $R(E_{c.m.})$ distribution for the $^{51}\text{V} + ^{159}\text{Tb}$ system.

The data treated as upper limits due to contamination by background events are represented with green points for $E_{c.m.} \geq 173.34$ MeV. The QE barrier distribution was derived from the $R(E_{c.m.})$ measurements [Fig. 6(b)] using a two-point difference formula similar to previous studies [15,16,18]:

$$D(E_i) = -\frac{R(E_{i+1}) - R(E_{i-1})}{E_{i+1} - E_{i-1}}. \quad (3)$$

TABLE I. List of parameters for the coupled-channel calculations [19] optimized to fit the measured experimental data.

Optical potential		
Real part		
$V_0 = 68$ MeV	$r_0 = 1.176$ fm	$a_0 = 0.689$ fm
Imaginary part		
$V_w = 45$ MeV	$r_w = 1.05$ fm	$a_w = 0.689$ fm
^{51}V excitation		
Quadrupole vibrational coupling		
$\beta_2 = 0.11$	$E_{1\text{ph}} = 0.320$ MeV	$N_{\text{ph}} = 1$
^{159}Tb excitation		
Quadrupole vibrational coupling		
$\beta_2 = 0.271$	$E_{1\text{ph}} = 0.058$ MeV	$N_{\text{ph}} = 1$
Rotational coupling		
$\beta_2 = 0.271$	$\beta_4 = 0.066$	$\beta_6 = -0.007$
Coupling of neutron-transfer reaction		
$F_{\text{tr}} = 0.05$	$Q = -0.821$ MeV	

The average barrier height, B_0 , can be obtained from the $R(E_{\text{c.m.}})$ distribution and corresponds to $R(B_0) = 0.5$. This value was evaluated using linear extrapolation between $E_{\text{c.m.}} = 159.37$ and 169.35 MeV in Fig. 6(a), giving

$$B_0 = 164.12 \pm 0.42 \text{ MeV}. \quad (4)$$

This value also corresponds to the maximum of the barrier distribution $D(E_{\text{c.m.}})$, as seen in Fig. 6(b) when $E_{\text{c.m.}} = B_0$.

D. Coupled-channel calculations

A comparison of the measured reflection probability $R(E_{\text{c.m.}})$ and barrier distribution $D(E_{\text{c.m.}})$ with coupled-channel calculations using the CCFULL [19] code helps to understand the reaction dynamics of the $^{51}\text{V} + ^{159}\text{Tb}$ system. In the calculation, the vibrational and rotational excitation of the ^{159}Tb target nucleus, the vibrational excitation of the ^{51}V projectile nucleus, as well as the coupling of the neutron transfer reaction, have been considered as a fully coupled system.

Table I lists the optimized parameters used for the coupled-channel calculations. The empirical formula from Akyüz and Winther [25] was used to calculate the initial values for optimizing the potential parameters (both real and imaginary). These parameters were then tuned to reproduce both the measured reflection probability $R(E_{\text{c.m.}})$ and barrier distribution $D(E_{\text{c.m.}})$ (Fig. 6).

The quadrupole vibrational coupling for both the target and projectile nuclei was also considered. The values of the excitation energies of the single-phonon $E_{1\text{ph}}$ were obtained

from the measured values of the first excited states of both nuclei. The quadrupole deformation parameter, β_2 , was derived from the measured value of the reduced quadrupole transition probability, $B(E_2)$ [26]. Furthermore, for the target nucleus, the rotational coupling due to the deformation up to the sixth order was also considered: β_2 , β_4 , and β_6 . However, the values of β_4 and β_6 were not based on experimental data but instead calculated using the finite-range droplet model (FRDM2012 [27]).

The Q value of the single neutron transfer reaction from ^{159}Tb to ^{51}V was determined based on the reported masses of the two nuclei, and its coupling strength, F_{tr} , was optimized to give the best fit to the experimental data.

Figure 6 also illustrates the impact of the quadrupole vibrational coupling and neutron transfer on the reproduction of the measured reflection probability $R(E_{\text{c.m.}})$ and QE barrier distribution $D(E_{\text{c.m.}})$. The dashed orange line corresponds to the calculations using the fully optimized set of parameters listed in Table I. The dashed purple line represents the CCFULL calculation with the same optimized parameters, but without considering either the quadrupole vibrational coupling of the target or projectile or the neutron transfer coupling. In addition, the dashed green line represents the result of the CCFULL calculation when only the quadrupole vibrational coupling of the target is considered.

Figure 6 highlights the importance of the deformation coupling in the $^{51}\text{V} + ^{159}\text{Tb}$ system. Both the target and projectile deformations need to be included fully to reproduce both $R(E_{\text{c.m.}})$ and $D(E_{\text{c.m.}})$. In the case of the projectile deformation coupling, the impact is less significant for the barrier distribution but should be considered to reproduce the low-energy part of $R(E_{\text{c.m.}})$.

The estimation of the barrier height of the side-collision configuration, B_{side} , was performed using the same procedure as in previous studies [15,16]. It was determined using the orientation-angle dependence of the Coulomb barrier height in the CCFULL code [19], with the optimized parameter listed in Table I. This was done by changing the angle θ of the collision between the projectile and the deformed target: $\theta = 0^\circ$ and $\theta = 90^\circ$ correspond to the tip collision and side-collision, respectively. The average entrance-channel barrier height B_0 is defined as follows:

$$B_0 = \int_0^{\pi/2} B(\theta) \sin \theta d\theta. \quad (5)$$

The side-collision configuration corresponds to the compact configuration with an angle $\theta = 90^\circ$. Using the same method as used by Tanaka *et al.* [15], the component of the reflection probability and the barrier distribution associated with the side-collision configuration can be extracted using the partial values $r_i(E_{\text{c.m.}})$ and $d_i(E_{\text{c.m.}})$ respectively:

$$r_i(E_{\text{c.m.}}) = \int_{\theta_{\text{min}}}^{\theta_{\text{max}}} r(E_{\text{c.m.}}, \theta) \sin \theta d\theta, \quad (6)$$

$$d_i(E_{\text{c.m.}}) = \frac{dr_i(E_{\text{c.m.}})}{dE_{\text{c.m.}}}. \quad (7)$$

The side-collision components correspond to an orientation angle between 80° and 90° . The orange dots in Fig. 6 represent the barrier distribution $d_{80^\circ-90^\circ}$, from which the value

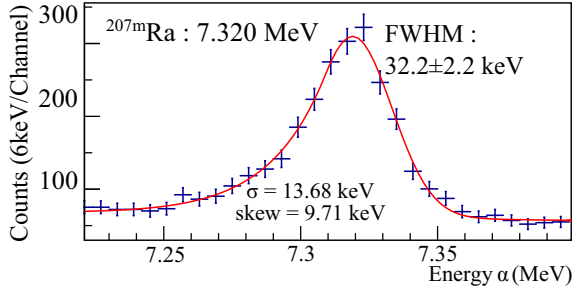


FIG. 7. A skewed Gaussian function fitted to the isomeric ^{207m}Ra α decay at 7.320 MeV. The fit parameters were then used in a global fit to the entire measured α spectrum, as shown in Fig. 8 (see text for details).

of B_{side} was extracted, denoted by the orange arrow corresponding to the maximum of the side-collision distribution. This value is approximately 4.4% higher than the measured value for B_0 and is equal to

$$B_{\text{side}} = 171.5 \pm 0.5 \text{ MeV}. \quad (8)$$

Both the average barrier height and side-collision energy (B_0 and B_{side}) will then be correlated with the measured excitation functions to determine whether the side-collision configuration effect observed in the SHE region is also present in lighter systems. The analysis of the excitation function is presented in the following sections.

IV. EXCITATION FUNCTION

A. Experimental method

For the measurement of the excitation functions for the $^{51}\text{V} + ^{159}\text{Tb} \rightarrow ^{210}\text{Ra}^*$ reaction, GARIS-III was used to transport the ER nuclei to the focal plane.

The detection and identification of the ER and their subsequent decays were performed using the GARIS-III detection setup. The estimation of the production yields of the several exit channels was based on the measurement of all their subsequent radioactive decays in the implantation detector, without decay-time selection. The analysis was performed using the total α spectrum produced at ten incident beam energies, each accumulated over 20 to 24 hours. Furthermore, between each measurement, an hour of beam off was systematically applied to remove cross-contamination in the α spectrum due to the longer-lived isotopes populated.

B. Data analysis

The α -decay events were selected in anticoincidence with both the TOF and veto signal to ensure the highest identification efficiency as well as the lowest background contamination possible. Both the timing and charge deposit information (TDC and QDC) of the TOF detector were used for this selection. In addition, only the DSSD spectrum was considered in the analysis. Indeed, the standalone resolution of the α spectrum of the DSSD is considerably better than that including the side detectors. The average resolution at 7.133

MeV for the DSSD is ≈ 32 keV (see Fig. 7) compared with ≈ 150 – 175 keV when using the side detectors.

This difference is due to the energy loss of the α particle in the dead layer when escaping the DSSD and entering the side detector. The restriction to the DSSD spectrum only limits the α -detection efficiency to $\approx 55\%$, rather than ≈ 85 – 88% when using the add-back correlation with the side detectors. However, this restriction ensures a better overall fit to the data thanks to the higher resolution and thus a cleaner measurement of the individual components in the α spectrum.

A skewed Gaussian function [28] was used to fit the α peaks to account for the actual detector response. Figure 7 shows the skew-Gaussian fit applied to the isomeric ^{207m}Ra α decay at 7.320 MeV with a measured FWHM of 32.2 ± 2.2 keV. The skew-Gaussian parameters extracted from this fit ($\sigma = 13.68$ keV and skewness = 9.71 keV) were fixed for all individual contributions used in the overall fitting of the α spectrum. Given the small range of α energies considered (5.5 to 7.5 MeV), these parameters should not change significantly and have been fixed for the stability of the fit.

The identification and the yield estimation, N_{0i} , of the individual exit reaction channels were based on the total α -energy spectrum measured at various beam energies, considering a wide range of evaporation channels (xn , pxn , αxn , ...). No decay-time selection was applied in the analysis, and the simulated/expected spectrum for each exit channel was considered using all decaying nuclides in the chain. For each isotope populated in the decay path of each exit channel, their reported decay characteristics (decay times and branching ratios) and respective reported uncertainties were considered in the simulation of the expected α -energy spectrum of each individual reaction channel. The experimental data inputs for the considered isotopes were taken from the NuDat database [29], and typical uncertainties considered in the fit were ± 15 keV for the α energy and $\pm 10\%$ for the reported branching ratios.

For each beam energy, the number of considered evaporation channels was tuned to include the maximum number of physically relevant reaction channels while ensuring the best and most stable fit possible to the α spectrum. Thus, not all evaporation channels were included in the fit at every beam energy. Furthermore, the isomeric (or excited state) decays were treated as separate exit channels from the ground-state (gs) decays because of their different decay paths.

However, in the estimation of the total cross section of the exit channels, their respective contributions were summed as follows: $N_{0i} = N_{0i}^{\text{gs}} + N_{0i}^e$. Figure 8 shows the overall fit to the total α spectrum measured at $E_{\text{c.m.}} = 170.13$ MeV. The solid black line represents the overall fit combining all the individual contributions of the reaction channels considered at this beam energy. Colored lines represent the contributions of individual reaction channels (ER_i), from which the yields were extracted. These yields, N_{0i} , were used to obtain the cross section of the different exit channels.

In addition, particular attention was given to the implantation profile of the different reaction residues measured in the DSSD. Indeed, a wide range of evaporation channels were produced and transported simultaneously, each with its own

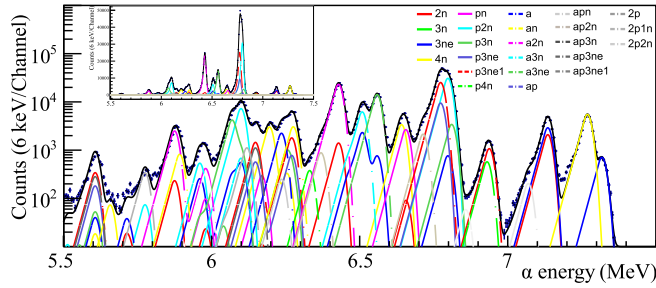


FIG. 8. Fit of the simulated spectrum to the measured total α spectrum at $E_{c.m.} = 170.13$ MeV on a logarithmic scale. The colored lines (solid and dashed) represent the individual contributions of the reaction channels considered at this beam energy. The solid black line represents the sum of all of contributions. The inset shows the fit on a linear scale.

magnetic rigidity $B\rho_i$. These differences in $B\rho_i$ resulted in a transmission dependence per reaction channel of up to 20%.

This dependence needed to be considered and corrected in the cross section estimation. However, due to the mixing of reaction channels in the α spectrum, the direct measurement of the implantation profile of the individual exit channels is impossible, making it difficult to apply simple and direct corrections.

However, by using the empirical formula introduced by Gregorich *et al.* [30], the equilibrium charge state in the helium gas and corresponding $B\rho$ of each evaporation residue can be estimated. This estimate is based on the average implantation energy measured in the DSSD (corrected for the pulse height defect), the mass, and the velocity of the individual ER at each beam energy.

In addition, the dispersion of GARIS-III at the focal plane is 19.8 mm/% [20]. Thus, by keeping one reaction channel centered in the DSSD at each energy point as a reference, the individual deviation from this reference for each reaction channel can be estimated. Based on these differences in $B\rho$ and the GARIS-III dispersion, the transmission of each individual exit channel can be corrected.

Figure 9 represents the reference channel selected at $E_{c.m.} = 158.74$ MeV used for this correction with the ^{207}Ra excited state decay. The implantation profile of the reference channel is plotted on the right panel in Fig. 9, and a Gaussian function (dashed red line) is used to obtain its centroid.

This method allows for the estimation of the transmission for individual evaporation residues (T_{ER_i}) at each beam energy. The nominal transmission was set at $70 \pm 15\%$ for the xn exit channels, based on the GARIS-III transmission characterization reported by Kaji *et al.* [20], and the reaction characteristics.

The second correction aspect concerns the disruption of the ER trajectory due to the emission of neutrons, protons, and alphas during the evaporation stage. This effect reduces the transmission of multiparticle exit channels because for some evaporation residues exiting the target the emission angle is larger than the angular acceptance of GARIS-III. Monte Carlo simulations were developed to estimate the effect of proton

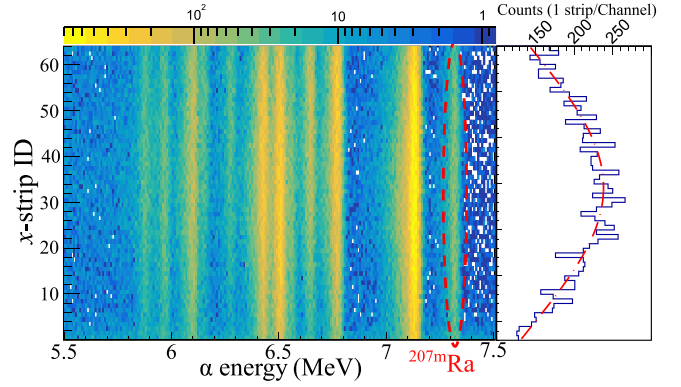


FIG. 9. Left panel: Total α -spectrum measurement at $E_{lab} = 210$ MeV as a function of the strip number along the dispersive axis of the separator. The dashed red ellipse shows the reference channel used at this beam energy for the $B\rho$ dispersion of the reaction products. Right panel: projection of the reference α decay channel, showing the implantation distribution of the ^{207m}Ra isotope. The dashed red line is the Gaussian fit to this distribution: FWHM $\approx 73.5 \pm 1.9$ strip.

and α -particle evaporation in the fusion-evaporation process based on the reaction kinematics.

These simulations considered the conservation of momentum in the center-of-mass frame. The internal barrier used for the kinetic energy of the proton and α -particle emission was taken from Parker *et al.* [31] The multiple scattering effect in the target for all ranges of ER was also considered in the simulations. The relative transmissions of all exit channels considered can be estimated and compared with the conventionally used xn channels, for which the transmission of GARIS-III was characterized [20]. The corrected transmissions were applied to the pxn and αxn channels in their cross section estimations.

C. Cross section estimation

The cross section of a given reaction channel is given by

$$\sigma_i = \frac{N_0 \times A_{Tb}}{\text{Dose} \times T_{ER_i} \times \mathcal{N}_A \times \rho_{Tb}}, \quad (9)$$

where N_0 and T_{ER_i} are the number of nuclei detected at the focal plane and the corrected transmission described in the previous section, respectively. A_{Tb} and ρ_{Tb} are the atomic number and density of the target, respectively, and \mathcal{N}_A is Avogadro's number. The dose is deduced from the number of Rutherford-scattered ^{51}V ions at the target position based on the detection geometry and beam energy.

In this study, the excitation functions of the xn , pxn and αxn reaction channels were measured simultaneously, as displayed in Fig. 10. In this experiment, a strong enhancement of the charged-particle evaporation channels was observed. The overall maximum cross section is $41.7 \pm 5 \mu\text{b}$ for the $\alpha 3n$ reaction channel at $E_{c.m.} = 177.7 \pm 1.5$ MeV, followed closely by the $p 3n$ channel with a cross section of $36.3 \pm 5 \mu\text{b}$ at $E_{c.m.} = 173.9 \pm 1.5$ MeV. The largest of the xn channels

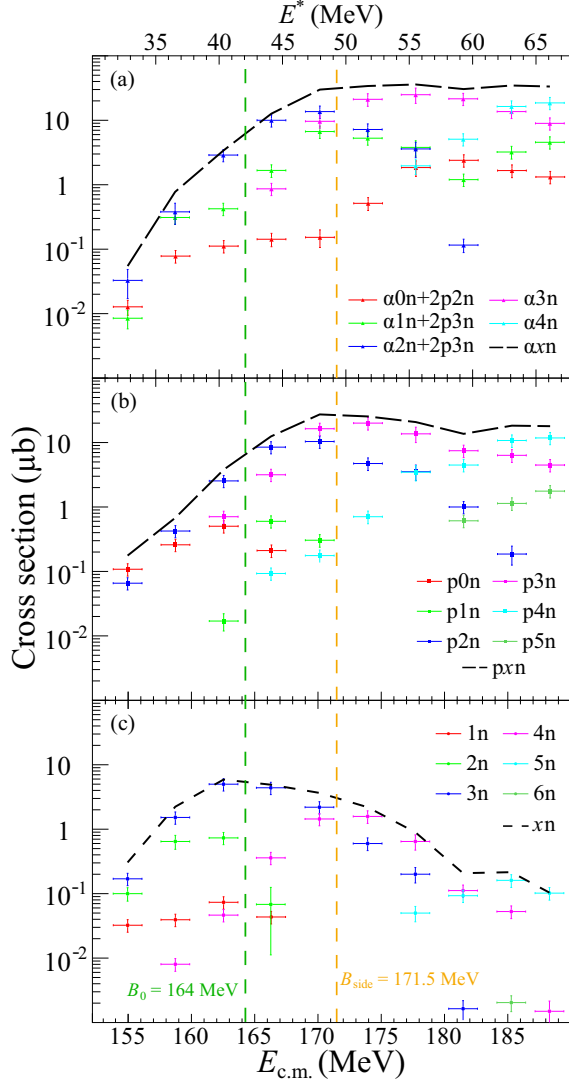


FIG. 10. Measured excitation functions for the $^{51}\text{V} + ^{159}\text{Tb}$ reaction: (a) αxn evaporation channels from $\alpha 0n$ to $\alpha 4n$, (b) pxn evaporation channels from $p 0n$ to $p 5n$, (c) xn evaporation channels from $1n$ to $6n$. The dashed black curves show the total measured cross sections for each reaction type. The vertical dashed lines represent the values of B_0 (green) and B_{side} (orange) obtained from the barrier distribution measurements and CCFULL calculation [19].

is the $3n$ channel with a cross section of only $4.7 \pm 1.5 \mu\text{b}$ at $E_{\text{c.m.}} = 162.5 \pm 1.5 \text{ MeV}$.

D. Correlation between the barrier distribution and the ER cross section

The average barrier height and side-collision energy are linked to the reaction dynamics and the maximum of the cross section. Moreover, as highlighted in previous studies in the SHE region [15,16], this relation is quite different for deformed and spherical targets. For deformed actinide targets, the maximum of the cross section is around the side-collision energy, whereas, for cold fusion reactions using spherical targets, it is around the average barrier height.

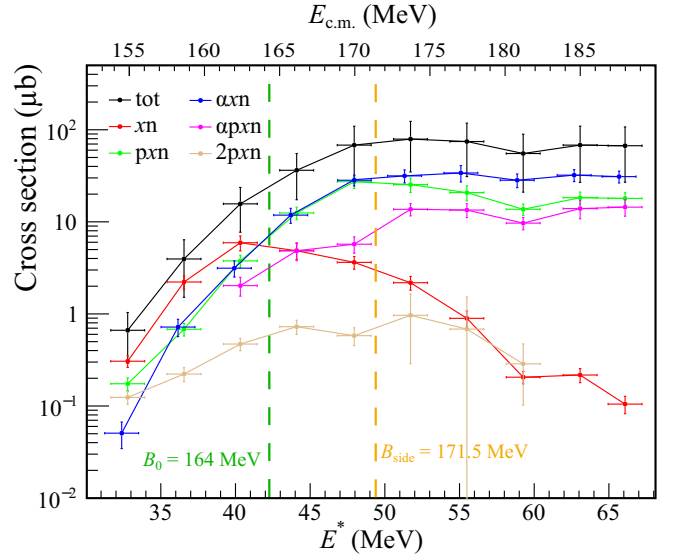


FIG. 11. Measured total cross sections: total evaporation-residue cross section in black, sum of the xn , pxn , αxn , αpxn , and $2pxn$ reaction channels in red, green, blue, pink, and light brown, respectively. The vertical dashed lines represent the values of B_0 (green) and B_{side} (orange) obtained from the barrier distribution measurements and CCFULL calculations [19].

In this measurement, the average barrier height B_0 is consistent with the maximum of the $3n$ evaporation channel and the side-collision energy B_{side} with the maximum of the $4n$. This phenomenon is consistent with the prediction and observation made by Hagino *et al.* [32]. However, the largest of the xn channels is the $3n$ channel, which is consistent with the average barrier height, even though ^{159}Tb is a deformed target.

Furthermore, the overall maximum of the cross section is not for any of the xn channels but for the $\alpha 3n$ channel at an energy 5 to 7 MeV higher than the side-collision energy (Fig. 10). Moreover, even if we consider the total cross section in Fig. 11, including all the measured reaction channels, the overall maximum is located around 174–176 MeV, or 3 to 5 MeV higher than the side-collision energy. However, both the $p 3n$ and the maximum of the pxn are close to the side-collision energy, with a maximum around 171 to 173 MeV.

The enhancement of the cross section for the xn channels around the side-collision energy observed in the SHE region with deformed actinide targets [16] is not observed in the studied reaction. The $^{51}\text{V} + ^{159}\text{Tb}$ system appears to behave more like fusion-evaporation reactions on spherical targets for xn channels. However, from these data alone, we cannot conclude if this behavior is specific to this system, to this region, or to the target/beam selected.

For a more systematic overview, we can investigate the reactions based on lighter ^{48}Ca and ^{50}Ti beams on ^{159}Tb targets studied at Texas A&M University [33,34].

However, no direct measurement of the barrier distribution has been performed for these reactions. The average barrier height B_0 can, however, be estimated. The diffused barrier formula [35] employed in the model used in the cross

TABLE II. Estimated average barrier heights, side-collision energies, and positions of the optimal bombarding energies for xn exit channels for ^{48}Ca , ^{50}Ti , $^{51}\text{V} + ^{159}\text{Tb}$ reactions. The underlined values correspond to the overall mid-target beam energies in the center-of-mass frame corresponding to the reported maximum cross sections for each reaction.

Beam	B_0 (MeV)	B_{side} (MeV)	E_{3n}^{max} (MeV)	E_{4n}^{max} (MeV)	E_{5n}^{max} (MeV)	E_{xn}^{max} (MeV)
^{48}Ca	≈ 142	$\approx 146\text{--}149$	≈ 140	≈ 150	<u>≈ 158</u>	≈ 157
^{50}Ti	≈ 158	$\approx 163\text{--}166$	≈ 158	<u>≈ 165</u>	≈ 174	≈ 161
^{51}V	164	≈ 171.5	<u>≈ 165</u>	≈ 172	≈ 185	≈ 165

section discussion (detailed in the next section) provided a very good reproduction of the measured B_0 for the $^{51}\text{V} + ^{159}\text{Tb}$ system. For ^{48}Ca and ^{50}Ti -induced reactions, the diffused barrier formula [35] gives mean barrier heights of 142 and 158 MeV in the center-of-mass frame, respectively. In addition, a rough estimation of the side-collision energy can be made at 3% to 5% higher energies based on the 4.4% measured in the case of the $^{51}\text{V} + ^{159}\text{Tb}$. From this assumption, for the $^{48}\text{Ca} + ^{159}\text{Tb}$ reaction, the side-collision energy could be around 146 to 149 MeV, and for the ^{50}Ti -induced reaction, the energy could be around 163 to 166 MeV. Furthermore, the maximum cross sections for all three reactions can be obtained from previous studies [33,34], and are listed in Table II along with the measurement performed in this study.

Based on the rough estimate of the side-collision energy and the xn measurement with different beams, a rough extended systematics of the relation of the optimal beam energy to the maximum cross section with a ^{159}Tb target can be extracted. Unfortunately, no clear trend can be observed from these three measurements. For the ^{48}Ca -induced reaction, the maximum cross section is the $5n$ channel at ≈ 158 MeV or around $B_{\text{side}} + 8$ MeV. For ^{50}Ti , the maximum is for the $4n$ channel at ≈ 165 MeV, or around the roughly estimated B_{side} . Finally, for the results presented in this study with ^{51}V , the largest of the xn exit channels is the $3n$ channel at ≈ 165 MeV or nearly the measured B_0 . A direct measurement of the barrier distribution is necessary to confirm this behavior and the side-collision energy for the Ca and Ti beams.

However, it appears that going from Ca to V, a transition in the optimal beam energy for the xn channels occurs: going from 6–7 MeV above the side-collision energy for ^{48}Ca to around the average barrier height for ^{51}V . This phenomenon might be associated with changes in fusion barriers, which result in varying fusion probabilities. According to the theoretical calculation, the fusion barrier should decrease with the asymmetry of the system: from the highest in the $^{51}\text{V} + ^{159}\text{Tb}$ system to the lowest for the $^{48}\text{Ca} + ^{159}\text{Tb}$ system. This phenomenon could result in a reduction of the fusion probabilities at higher excitation energies for the ^{51}V and ^{50}Ti systems compared with the ^{48}Ca systems, leading to the observed reduction in optimal beam energy for xn channels.

Additional measurements using a ^{51}V projectile and Ho, Gd, Dy, or Er targets could also be useful to extend these systematic studies and to understand better the reaction mechanism. Such studies could also confirm or deny the strong enhancement of the charged-particle emission observed in this study.

V. THEORETICAL CALCULATIONS

A. Comparison with lighter beams

The analysis of the $^{51}\text{V} + ^{159}\text{Tb}$ reaction provides an unique opportunity to assess the influence of entrance-channel effects on the fusion probability when changing the projectile from ^{48}Ca to a heavier one while keeping the same deformed target.

In the analysis of excitation functions, we will assume, as in models of heavy and superheavy nuclei synthesis, that the process occurs in three independent steps [36]. The first step is the capture of the projectile by the target. The second step describes fusion, i.e., the transition from a strongly interacting composite system to a compound nucleus configuration. The third and final stage describes the cooling process through the emission of neutrons, light-charged particles (LCPs), and γ rays or fission. The cross section for the formation of the final evaporation residue in reaction channel i can be expressed as

$$\sigma_i = \pi \lambda^2 \sum_{\ell=0}^{\infty} (2\ell + 1) \times T_{\ell} \times P_{\text{fus}} \times W_i, \quad (10)$$

where P_{fus} and W_i are the probabilities of fusion and survival, respectively. The capture cross section $\sigma_{\text{cap}} = \pi \lambda^2 \sum_{\ell=0}^{\infty} (2\ell + 1) \times T_{\ell}$, where T_{ℓ} is the entrance-channel barrier transmission coefficient, the squared reduced wavelength $\lambda^2 = \frac{\hbar^2}{2\mu E_{\text{c.m.}}}$, and μ is the reduced mass of the colliding system. For convenience, the dependencies of the components of Eq. (10) on angular momentum ℓ and energy have been omitted here.

The comparative analysis of the ^{48}Ca , ^{50}Ti , $^{51}\text{V} + ^{159}\text{Tb}$ reactions will begin with a discussion of the total cross sections $\sum \sigma_{xn}$ for the xn channels, as presented in Fig. 12. Additionally, the figure presents data for the $^{40}\text{Ar} + ^{166}\text{Er} \rightarrow ^{206-x}\text{Rn} + xn$ ($x = 3, 4, \text{ and } 5$) reaction recently measured by Chernysheva *et al.* [37]. It is worth noting that the evaporation cascades in the xn channels of the excited $^{209}\text{Fr}^*$, $^{206}\text{Rn}^*$, and $^{207}\text{At}^*$ nuclei directly overlap with the measured $p xn$ and αxn (or $2p yn$, $y \geq 2$) channels, and partially with the $\alpha p xn$ cascade of $^{210}\text{Ra}^*$.

In Fig. 12, vertical arrows indicate the excitation energies corresponding to collisions at $E_{\text{c.m.}} = B_0$ for each reaction (see Table II). For the $^{51}\text{V} + ^{159}\text{Tb}$ and $^{40}\text{Ar} + ^{166}\text{Er}$ reactions, data are available down to approximately 8 MeV below the entrance-channel barrier. For the other two reactions, measurements were taken only at above-barrier energies. Several MeV above the barrier, the full range of partial waves contributing to fusion for each reaction is already achieved, and the fusion cross section σ_{fus} saturates. For excitation

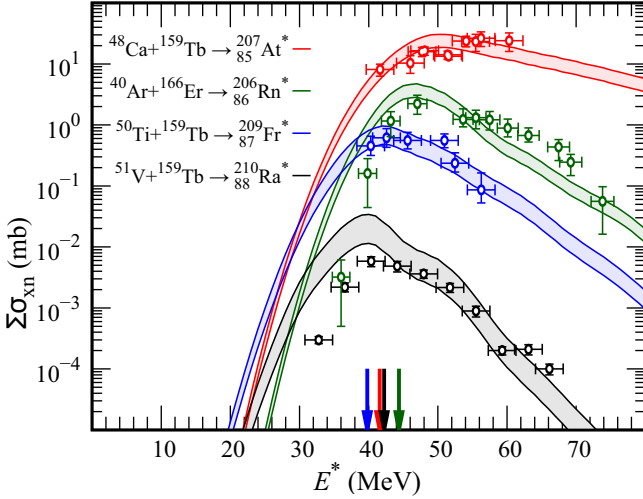


FIG. 12. Total xn cross sections, $\sum \sigma_{xn}$, for the ^{48}Ca , ^{50}Ti , $^{51}\text{V} + ^{159}\text{Tb}$, and $^{40}\text{Ar} + ^{166}\text{Er}$ reactions. Vertical arrows indicate the excitation energies corresponding to collisions at $E_{c.m.} = B_0$ for each reaction. The colored bands show the range of model calculations.

energies around 50 MeV, experimental data show that changing the projectile from ^{48}Ca to ^{50}Ti causes a decrease in the cross section by a factor of approximately 50. A subsequent change from ^{50}Ti to ^{51}V results in a further reduction by a factor of approximately 100. For energies higher by an additional 10 MeV, the difference in cross sections between the $^{48}\text{Ca} + ^{159}\text{Tb}$ and $^{51}\text{V} + ^{159}\text{Tb}$ reactions exceeds five orders of magnitude.

It is also interesting to compare the cross section for the $^{51}\text{V} + ^{159}\text{Tb}$ reaction with that for $^{40}\text{Ar} + ^{166}\text{Er}$, which leads to a compound nucleus differing by an α particle. In this case, the cross section at energies well above the barrier differs by three orders of magnitude. This value aligns with the empirical systematics proposed by Hinde and Dasgupta in [38] for a wide range of reactions. A similar effect of a 1000-fold increase in the cross section between reactions leading to ^{212}Th and ^{208}Ra nuclei was discussed therein, explaining it in terms of the emission of charged particles before the formation of a compact compound nucleus.

However, when comparing the results for $^{51}\text{V} + ^{159}\text{Tb}$ with the measurements of $^{44}\text{Ca} + ^{162}\text{Dy} \rightarrow ^{206-x}\text{Ra} + xn$ ($x = 3, 4, 5$) reported by Werke *et al.* [39], the relative differences are smaller. Cross sections reported by Werke *et al.* were approximately a factor of ten lower compared with those for $^{40}\text{Ar} + ^{166}\text{Er}$. These differences may result from a greater charge symmetry between projectile and target in the $^{44}\text{Ca} + ^{162}\text{Dy}$ reaction, leading to a less favorable fusion probability. However, this issue has not yet been discussed in detail and requires further investigation.

At energies above the barrier, the observed differences between reactions of ^{48}Ca , ^{50}Ti , and ^{51}V beams with a ^{159}Tb target result from the combination of two factors: fusion probability and survival probability. The key issue is determining the extent to which these differences arise from entrance-channel effects compared to statistical effects. In the following section, we discuss model calculations depicted in Fig. 12,

which effectively describe these and other experimental data.

B. Statistical model

To calculate the capture cross section in Eq. (10), the “dif-fused barrier formula” is used, assuming a Gaussian shape for the entrance-channel barrier [35]. The formula provides the absolute value of the capture cross section σ_{cap} for a given energy $E_{c.m.}$ or the maximum value of angular momentum ℓ_{max} to be used in Eq. (10) in the sharp cutoff approximation, where $T_\ell = 1$ for $\ell \leq \ell_{\text{max}}$ and zero otherwise. The same method for determining σ_{cap} was used by Mayorov *et al.* [33,34] in the analysis of reactions of ^{48}Ca and ^{50}Ti with a ^{159}Tb target. Here, the parametrization of the mean barrier height B_0 and its width ω given in Ref. [40] is used. For the $^{51}\text{V} + ^{159}\text{Tb}$ reaction, this parametrization yields a barrier height consistent with the experimental measurements, $B_0 = 164.39$ MeV. In addition, the calculated width of the barrier, $\omega = 4.94$ MeV, is also not too far from the measured one of 6.78 MeV.

The fusion probability in Eq. (10) is not a directly measurable quantity, and there is no single established method for its calculation. However, in many cases, the average fusion probability, $\langle P_{\text{fus}} \rangle$, can be estimated experimentally. Numerous measurements of heavy-ion fusion reactions leading to nuclei heavier than Pb showed that $\langle P_{\text{fus}} \rangle$ is close to unity only for the most charge asymmetric reactions [41]. Reduction of the fusion cross section caused by so-called quasifission is present even for relatively asymmetric reactions, such as $^{19}\text{F} + ^{197}\text{Au}$ ($\langle P_{\text{fus}} \rangle = 0.65 \pm 0.09$ [42]) or $^{22}\text{Ne} + ^{194}\text{Pt}$ ($\langle P_{\text{fus}} \rangle \approx 0.30\text{--}0.45$ [43]), both leading to $^{216}\text{Ra}^*$. For more symmetric systems such as ^{48}Ca , ^{50}Ti , $^{51}\text{V} + ^{159}\text{Tb}$, the expected effect is larger, especially for sub-barrier energies.

In general, the fusion probability depends on angular momentum; however, for the systems under consideration, the projectile-target contact configuration is typically quite close to the fusion saddle point. For energies above the entrance-channel barrier, the moments of inertia of both configurations are comparable, and the differences in rotational energies do not significantly raise the fusion barrier, even for higher partial waves. As a result, the fusion probability does not show strong dependence on ℓ and can be replaced by an average value in Eq. (10). This is supported by multiple experimental data for $\sum \sigma_{xn}$, which are usually well described using $\langle P_{\text{fus}} \rangle$ when $E_{c.m.} > B_0$ [38]. For energies below the barrier, the merging process begins at more elongated configurations (like the tip-to-tip configuration), and the fusion probability is usually lower than $\langle P_{\text{fus}} \rangle$. In the current analysis we consider $\langle P_{\text{fus}} \rangle$ as a scaling parameter for the calculations, so that they best reproduce the experimental data. The last term in Eq. (10), the survival probability, is calculated using standard Monte Carlo methods employed in statistical models. We assume that deexcitation can occur through fission or through the emission of neutrons, LCPs (p and α particles), and γ rays (but only at low excitation energies, below the fission and particle thresholds). In the adopted model, the decay widths for neutron and charged-particle emission are calculated using

the Weisskopf formula,

$$\Gamma_j = \frac{g_j m_j}{\pi^2 \hbar^2 \rho_{g.s.}} \int_0^{X_j} \sigma_{inv}^j(\epsilon_j) \rho_j(X_j - \epsilon_j) \epsilon_j d\epsilon_j, \quad (11)$$

where j represents a n, p, or α particle. The fission width is calculated using an expression from transition-state theory,

$$\Gamma_f = \frac{1}{2\pi \rho_{g.s.}} \int_0^{X_f} \rho_f(X_f - \epsilon_f) d\epsilon_f, \quad (12)$$

where ϵ_j and ϵ_f are the kinetic energies carried away by the emitted particle and the two fission fragments, respectively. The integral upper bounds, $X_j = \epsilon^* - B_j - E_{rot}^j$ and $X_f = \epsilon^* - B_f - E_{rot}^f$, are the maximum available energies for particle emission or for fission fragments. Here, ϵ^* is the excitation energy of the nucleus under consideration in the cascade, B_j and B_f represent the particle binding energy and the fission barrier height, while E_{rot}^j and E_{rot}^f are the rotational energies of the daughter nucleus after particle emission and of the fission saddle point, calculated for rigid bodies.

In Eq. (11), the parameters g_j and m_j represent the particle spin degeneracy and its mass, respectively. The barrier heights, V_p and V_α , for proton and α -particle emission are taken from Parker *et al.* [31], while for neutrons $V_n = 0$. The cross section for particle capture in the inverse process is zero for $\epsilon_j \leq V_j$ and $\sigma_{inv}^j(\epsilon_j) = (1 - \frac{V_j}{\epsilon_j}) \sigma_{geo}^j$ otherwise, where σ_{geo}^j is the geometrical cross section.

In both formulas, Eqs. (11) and (12), $\rho_{g.s.}$ is the level density of the nucleus under consideration calculated at its thermal excitation energy (ϵ^* reduced by g.s. rotational energy), while $\rho_j(\dots)$ and $\rho_f(\dots)$ are the level densities of the daughter nucleus and at the saddle-point configuration, respectively. The individual level densities are calculated using the formula

$$\rho(U) = \frac{\sqrt{\pi}}{12} \frac{2\sqrt{a(U-P)}}{a^{1/4}(U-P)^{5/4}}, \quad (13)$$

where the thermal excitation energy U at which level densities are evaluated is shifted by the pairing energy P . In the calculations, we use deformation-dependent level density parameters a , calculated using the formulas proposed by Reisdorf [44], with shell effects accounted for by the Ignatyuk formula with a standard damping energy of 18.5 MeV [45].

The Monte Carlo method is used to evaluate the survival probability W_i for a given channel j . The probability of a given process (fission or emission of particle j) is given by the ratio of its decay width to the total decay width. After each successful particle emission, the excitation energy is reduced by the particle's binding energy and its kinetic energy. The kinetic energy is randomly selected from the distribution resulting directly from the level density distribution for the process. Spin reduction is not considered. The cascade ends when the available energy is below the fission and particle thresholds or the system undergoes fission.

Numerical values of parameters and constants used in the model and additional details are listed in Refs. [40,46]. Experimentally known masses from AME2020 were used when available [47,48]. All other masses and fission barrier heights were taken from the tables by Möller *et al.* [27,49].

Ground-state deformations were adopted from [27], while saddle point deformations were obtained using the macroscopic-microscopic model by Jachimowicz *et al.* [50].

The above definition of the model is quite minimalistic. However, this approach allows us to examine the influence of various parameters and potential later deliberate modifications, such as the introduction of Kramers-Strutinsky factors or collective enhancement of level density (CELD). The impact of these commonly used effects on the calculations are discussed later.

C. Model calibration

In the case of complex evaporation cascades, it is necessary to consider the properties of even several dozen different nuclides in the calculations. Of all the input data, the calculations are most sensitive to the heights of the fission barriers and the method of calculating the saddle point level densities. A common practice is to modify the fission barriers (especially the macroscopic part) to achieve agreement with the measured cross sections [51]. Such a practice is justified in the studied region of nuclei for several reasons. In the tables by Möller *et al.* [49], the barrier heights are given relative to the potential energy minimum, for which the shape of the system is most stable with respect to fission at zero excitation energy. Calculations [27] indicate that, for almost all nuclei that need to be considered in the $^{210}\text{Ra}^*$ evaporation cascade, the ground-state shapes exhibit a slightly oblate ($-0.20 < \beta_{20}^{gs} \leq -0.10$) or oblate deformation ($\beta_{20}^{gs} \leq -0.20$). However, similarly to the actinides, the analysis of potential energy maps for light Ra, Fr, and Rn nuclei indicates the existence of additional local minima, often with a prolate shape, that can be populated during the reaction or must be crossed on the way to fission. The fission barrier heights for these minima may be significantly lower. Such effects cannot be unambiguously accounted for in statistical calculations; therefore, introducing a reduced barrier height might improve the agreement with experimental data. Therefore, we will introduce a scaling factor for the fission barrier heights, c_f and assume that the effective fission barrier height $B_f = c_f \times B_f^{\text{tab}}$, where B_f^{tab} is the tabulated value.

To test the model and estimate scaling factors for barrier heights, we first examined reactions leading to various isotopes of Po, At, Rn, Fr, Ra in the xn channels, for which $P_{\text{fus}} = 1$ or the fusion probability is experimentally known.

These reactions were $^{12}\text{C} + ^{194,198}\text{Pt} \rightarrow ^{206,210}\text{Po}^*$ [54], $^{12}\text{C} + ^{197}\text{Au} \rightarrow ^{209}\text{At}^*$ [52], $^{16}\text{O} + ^{194}\text{Pt} \rightarrow ^{210}\text{Rn}^*$ [55], $^{16}\text{O} + ^{197}\text{Au} \rightarrow ^{213}\text{Fr}^*$ [52], $^{18}\text{O} + ^{197}\text{Au} \rightarrow ^{215}\text{Fr}^*$ [56], $^{12}\text{C} + ^{204}\text{Pb} \rightarrow ^{216}\text{Ra}$ [42], $^{19}\text{F} + ^{197}\text{Au} \rightarrow ^{216}\text{Ra}$ [42], $^{30}\text{Si} + ^{186}\text{W} \rightarrow ^{216}\text{Ra}$ [42], and $^{22}\text{Ne} + ^{194}\text{Pt} \rightarrow ^{216}\text{Ra}$ [43].

Satisfactory agreement with the data was achieved by reducing the barrier heights from the tables by 10% for Rn and Fr nuclei ($c_f = 0.9$). The same scaling factor was applied to Ra nuclei with mass numbers $A > 210$. However, for nuclei with $A \leq 210$, a scaling factor of $c_f = 0.8$ was used, which will be justified soon. There was no need to scale the barriers for Po and At nuclei. Barrier heights for lighter elements also remained unchanged. In Figs. 13 and 14, a comparison of measured cross sections for selected reactions with model

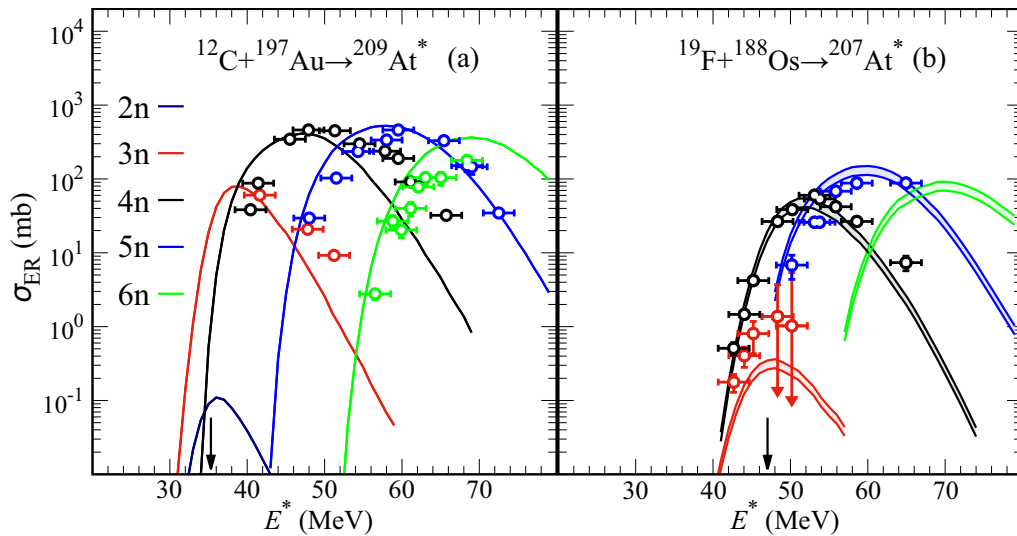


FIG. 13. Comparison of model calculations with experimentally measured cross sections for reactions (a) $^{12}\text{C} + ^{197}\text{Au} \rightarrow ^{209}\text{At}^*$ [52] ($\langle P_{\text{fus}} \rangle = 1$) and (b) $^{19}\text{F} + ^{188}\text{Os} \rightarrow ^{207}\text{At}^*$ [53] ($\langle P_{\text{fus}} \rangle = 0.65 \pm 0.09$). Vertical arrows indicate the excitation energies corresponding to collisions at $E_{\text{c.m.}} = B_0$.

calculations is presented. In Fig. 13, reactions leading to $^{201-206}\text{At}$ are shown. For the $^{12}\text{C} + ^{197}\text{Au}$ reaction, $P_{\text{fus}} = 1$ was assumed. For the $^{19}\text{F} + ^{188}\text{Os}$ reaction measured by Mahata *et al.* [53], the estimated fusion probability is $\langle P_{\text{fus}} \rangle = 0.65 \pm 0.09$, which is the same as the experimentally determined value for the $^{19}\text{F} + ^{197}\text{Au} \rightarrow ^{216}\text{Ra}^*$ reaction in Ref. [41].

The estimated value is consistent with $\langle P_{\text{fus}} \rangle = 0.63$ obtained by Banerjee *et al.* [57]. For the $^{48}\text{Ca} + ^{159}\text{Tb}$ reaction in Fig. 14, the estimated value is $\langle P_{\text{fus}} \rangle = 0.20 \pm 0.05$. This value is in agreement with the value calculated using the empirical parametrization used by Mayorov *et al.* [33] in their analysis of this reaction, yielding a fusion probability of 0.16 at $E_{\text{c.m.}} = B_0$, and is close to the value of 0.28 obtained by Banerjee *et al.* [57].

It should be noted that even relatively small uncertainties in adopted masses, and especially fission barriers, can cause deviations of model calculations from experimental

data reaching an order of magnitude (see for instance the discussion by Loveland in Ref. [58]). Within the adopted assumptions, the calculations reasonably reproduced experimental data with an accuracy of a factor of three to five, which we take as a rough estimate of the uncertainty of the statistical part of the model. To illustrate these uncertainties, all excitation functions will be shown with error corridors, which result from the limits of the adopted $\langle P_{\text{fus}} \rangle$ values.

In Fig. 14, two reactions, $^{40}\text{Ar} + ^{166}\text{Er}$ and $^{50}\text{Ti} + ^{159}\text{Tb}$, leading to the compound nuclei $^{206}\text{Rn}^*$ and $^{209}\text{Fr}^*$ are presented. For the $^{40}\text{Ar} + ^{166}\text{Er}$ reaction, the estimated fusion probability is the same as for the $^{48}\text{Ca} + ^{159}\text{Tb}$ reaction, 0.20 ± 0.05 . However, for the $^{50}\text{Ti} + ^{159}\text{Tb}$, the fusion probability decreases by an order of magnitude to $\langle P_{\text{fus}} \rangle = 0.03 \pm 0.01$. Again, these values are in reasonable agreement with the empirical parametrization in Ref. [33], yielding fusion probabilities of 0.22 and 0.07 at $E_{\text{c.m.}} = B_0$, respectively.

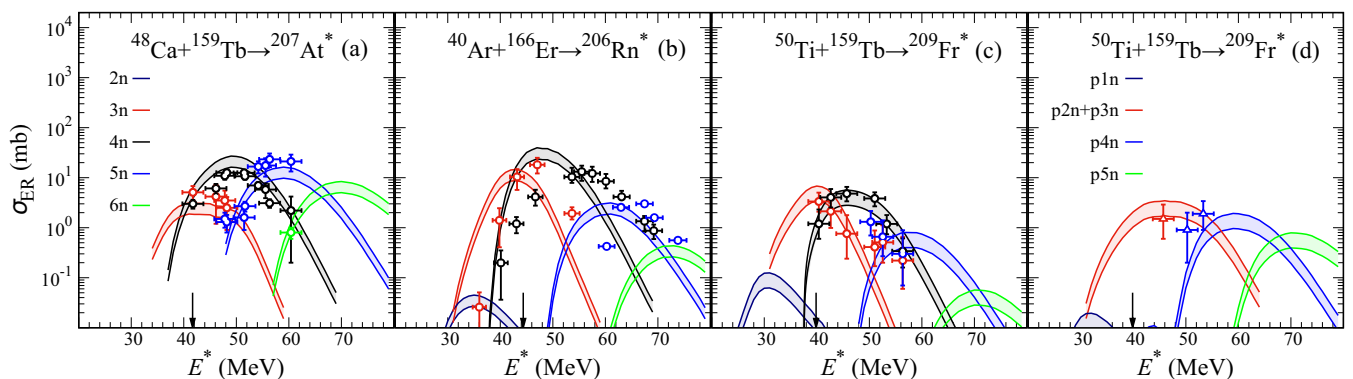


FIG. 14. Comparison of model calculations with experimentally measured cross sections for reactions (a) $^{48}\text{Ca} + ^{159}\text{Tb} \rightarrow ^{209}\text{At}^*$ [33] ($\langle P_{\text{fus}} \rangle = 0.20 \pm 0.05$), (b) $^{40}\text{Ar} + ^{166}\text{Er} \rightarrow ^{206}\text{Rn}^*$ [37] ($\langle P_{\text{fus}} \rangle = 0.20 \pm 0.05$), (c) and (d) $^{50}\text{Ti} + ^{159}\text{Tb} \rightarrow ^{209}\text{Fr}^*$ [34] ($\langle P_{\text{fus}} \rangle = 0.03 \pm 0.01$). Vertical arrows indicate the excitation energies corresponding to collisions at $E_{\text{c.m.}} = B_0$.

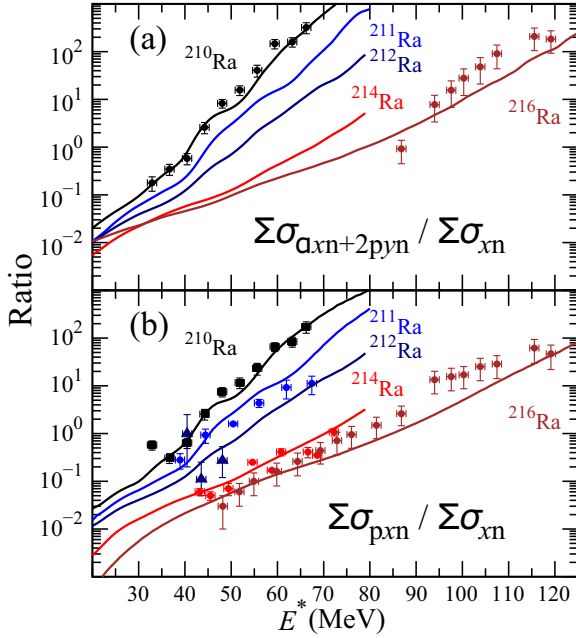


FIG. 15. Ratios of measured cross sections, (a) $\sum \sigma_{\alpha xn+2pyn} / \sum \sigma_{xn}$ (where $y \geq 2$) and (b) $\sum \sigma_{pxn} / \sum \sigma_{xn}$, for ^{210}Ra ($^{51}\text{V} + ^{159}\text{Tb}$), ^{211}Ra ($^{40}\text{Ar} + ^{171}\text{Yb}$ [60]), ^{212}Ra ($^{50}\text{Ti} + ^{162}\text{Dy}$ [34]), ^{214}Ra ($^{40}\text{Ar} + ^{174}\text{Yb}$ [60]), and ^{216}Ra ($^{22}\text{Ne} + ^{194}\text{Pt}$ [59]). Statistical model calculations are represented by solid lines.

For the $^{50}\text{Ti} + ^{159}\text{Tb}$ reaction, the pxn channels shown in panel (f) are reasonably reproduced. Unfortunately, in Refs. [33,34,37,53], no information is available about other pxn or αxn channels, although according to model calculations, such channels could be observed at an order of magnitude lower cross sections than xn channels. The total cross sections $\sum \sigma_{xn}$ for the $^{48}\text{Ca} + ^{159}\text{Tb}$, $^{40}\text{Ar} + ^{166}\text{Er}$, and $^{50}\text{Ti} + ^{159}\text{Tb}$ reactions from Fig. 13 are presented in Fig. 12.

D. Channels with LCPs

In this section, we will provide an explanation for the observed enhancement of the pxn and αxn channels in the $^{51}\text{V} + ^{159}\text{Tb}$ reaction. Unfortunately, there is not much information in the literature about the αxn channels in reactions leading to radium nuclei. We are aware only of $\alpha 8n$ - $\alpha 12n$ channels reported at very high excitation energies by Andreyev *et al.* [59] in reactions between ^{22}Ne and $^{194,196,198}\text{Pt}$. However, there are several reactions for which the pxn cross sections are known. Here, we will consider the following reactions: $^{22}\text{Ne} + ^{194}\text{Pt} \rightarrow ^{216}\text{Ra}^*$ [59], $^{40}\text{Ar} + ^{171,174}\text{Yb} \rightarrow ^{211,214}\text{Ra}^*$ [60], and $^{50}\text{Ti} + ^{162}\text{Dy} \rightarrow ^{212}\text{Ra}^*$ [34]. To study the enhancement of channels with charged particles relative to channels with neutron emission only, in Fig. 15 we present the ratios

$$\frac{\sum \sigma_{\alpha xn+2pyn}}{\sum \sigma_{xn}} \approx \frac{\sum_{\ell=0}^{\ell_{\max}} (2\ell+1) W_{\alpha xn+2pyn}}{\sum_{\ell=0}^{\ell_{\max}} (2\ell+1) W_{xn}}, \quad (14)$$

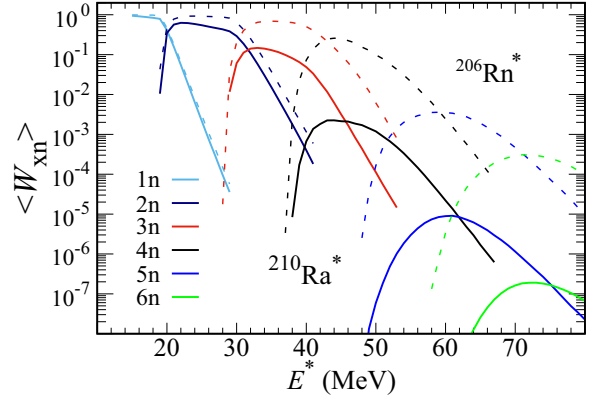


FIG. 16. Survival probabilities $\langle W_{xn} \rangle$ averaged over ℓ , for consecutive xn channels for $^{210}\text{Ra}^*$ (solid lines) and $^{206}\text{Rn}^*$ (dashed lines) excited nuclei.

where $y \geq 2$, and

$$\frac{\sum \sigma_{pxn}}{\sum \sigma_{xn}} \approx \frac{\sum_{\ell=0}^{\ell_{\max}} (2\ell+1) W_{pyn}}{\sum_{\ell=0}^{\ell_{\max}} (2\ell+1) W_{xn}}. \quad (15)$$

The experimental ratios are approximately equal to ratios of statistical model calculations when P_{fus} is used instead of ℓ -dependent P_{fus} in Eq. (10). This provides a powerful test for the evaporation cascade calculations, because these ratios do not depend on the fusion cross section. They can also help identify preequilibrium emission of light-charged particles, as suggested by Hinde and Dasgupta in Ref. [38].

The $\sum \sigma_{pxn} / \sum \sigma_{xn}$ ratios in Fig. 15(b) for $^{216}\text{Ra}^*$ and $^{214}\text{Ra}^*$ deexcitation cascades show no enhanced proton emission effect up to 70–80 MeV of excitation energy. However, when departing from the closed neutron shell $N = 126$, the pxn channels become more dominant. We can clearly observe a systematic increase in channels with proton emission with decreasing mass number of the first nucleus in the cascade. All ratios exhibit an exponential increase with energy. Above 60 MeV, the $\sum \sigma_{pxn} / \sum \sigma_{xn}$ ratio for the $^{210}\text{Ra}^*$ cascade exceeds 100 and is comparable to the ratio for $^{216}\text{Ra}^*$ at a much higher energy of 120 MeV. Surprisingly, the model calculations describe all these effects well. The $\sum \sigma_{\alpha xn+2pyn} / \sum \sigma_{xn}$ ratios in Fig. 15(a) for $^{216}\text{Ra}^*$ and $^{210}\text{Ra}^*$ deexcitation cascades are also well reproduced. The radical change in the decay mode of excited Ra nuclei departing from the closed neutron shell indicates a strong isotopic effect. We argue that this effect is caused by significantly lower fission barriers in the Ra isotopic chain compared to neighboring Fr and Rn chains. The enhancement of the αxn channels can be explained by analyzing the averaged survival probabilities in the xn channels for ^{210}Ra and ^{206}Rn , as presented in Fig. 16. A similar explanation can be given for the enhancement of the pxn channels.

Typically, the probability of emitting a charged particle from the hot heavy nuclei considered here at equilibrium is smaller by at least one or two orders of magnitude compared with the probability of emitting a neutron. Such emissions usually occur at the beginning of the cascade when the excitation energy is still high. For $^{210}\text{Ra}^*$ at the maximum of

the $3n$ reaction channel the average angular momentum (in the sharp cut-off approximation) $\langle \ell \rangle \approx 9\hbar$ ($E^* = 40$ MeV), while at the maximum of the $\alpha 3n$ reaction channel $\langle \ell \rangle \approx 34\hbar$ ($E^* = 55$ MeV). The states from which α particles are emitted are not close to the yrast states, and the probability of α -particle emission should not depend strongly on angular momentum [61]. It is not excluded that some effects related to angular momentum might play a role in enhancing α -particle emission; however, no additional mechanisms are considered in the calculations.

For a numerical example, let us assume that an α particle is emitted from $^{210}\text{Ra}^*$ at $E^* = 60$ MeV as the first particle with a probability of 0.01. The resulting nucleus is $^{206}\text{Rn}^*$ at $E^* \approx 45$ MeV, for which the survival probability at this energy is more than 10% in the $4n$ channel due to high fission barriers (see the dashed black curve in Fig. 16). This makes the survival probability for $^{210}\text{Ra}^*$ in the $\alpha 4n$ channel approximately 10^{-3} , which is two orders of magnitude higher than the value for the $5n$ channel (solid blue line). The rapid decline in $\langle W_{xn} \rangle$ for each subsequent neutron emission in the Ra cascade is attributed to the decreasing fission barriers as A decreases.

According to Möller *et al.* [49], the fission barriers for the Ra isotopic chain progressively decline from a peak of 15 MeV, one neutron below the closed shell $N = 126$, to less than 7 MeV for nuclei with ten fewer neutrons. For the Fr isotopic chain all fission barriers are typically 2 MeV higher, and for Rn they are usually more than 4 MeV higher. The scaling factors c_f determined in the model calibration suggest that these differences are even greater, and the decline in fission barriers in the Ra isotopic chain is steeper. This explains why the enhancement of pxn and αxn channels becomes more pronounced as the mass number of the initial nucleus in the cascade in Fig. 15 decreases. As fission competition increases, the likelihood of survival in the xn channels diminishes, resulting in the path involving LCP emission becoming more favorable.

E. CELD

An effect similar to that of reducing the fission barriers can be achieved by introducing collective enhancement of level density (CELD). This option requires verification. CELD involves modifying the level density, $\rho(U)$, as defined by Eq. (13), to include rotational and vibrational states. The enhanced level density is assumed to be $\rho'(U) = K_{\text{coll}}\rho(U)$, where the factor K_{coll} includes rotational (K_{rot}) and vibrational (K_{vib}) components, which depend on the shape of the nucleus and its temperature.

There is no universally accepted method for incorporating collective effects. We will utilize formulas from the work of Zagrebaev *et al.* [62], the NRV code [63], and original work by Junghans *et al.* [64]. Similar methods are also employed in the KEWPIE2 code [65] and have been adopted by Mayorov *et al.* [33,34] in the analysis of the $^{48}\text{Ca} + ^{159}\text{Tb}$ and $^{50}\text{Ti} + ^{159}\text{Tb}$ reactions. However, there are also works that do not support the use of CELD. For instance, Komarov *et al.* [66] reported issues with reproducing an α -particle spectrum, and Sagaidak *et al.* [67] faced difficulties in explaining the deexcitation of different isotopes of Po when CELD was applied in calculations.

Following Junghans *et al.* [64], we will assume that for spherical shapes $K_{\text{rot}} = 1$, and for deformed shapes

$$K_{\text{rot}} = \begin{cases} (\sigma_{\perp}^2 - 1)f(U) + 1, & \sigma_{\perp}^2 > 1, \\ 1, & \sigma_{\perp}^2 \leq 1, \end{cases} \quad (16)$$

where the squared spin-cutoff parameter $\sigma_{\perp}^2 = \frac{I_{\perp}T}{\hbar^2}$. Here, I_{\perp} is the perpendicular moment of inertia, and T is the temperature.

The vibrational factor depends on the nucleus under consideration, and its calculation method is phenomenological in nature. Here, we will adopt the formula

$$K_{\text{vib}} = \exp\{0.0555A^{2/3}(T/\text{MeV})^{4/3}\}f(U), \quad (17)$$

which is used in the NRV and KEWPIE2 codes [63,65].

In Eqs. (16) and (17), the function $f(U)$ describes the damping of collective excitations with increasing excitation energy. We will use a formula proposed by Junghans *et al.* [64], adjusted as a function of the thermal energy U shifted by the pairing energy P : $f(U) = [1 + \exp\{\frac{(U-P)-E_{\text{crit}}}{d_{\text{crit}}}\}]^{-1}$, where the parameters $E_{\text{crit}} = 40$ MeV, $d_{\text{crit}} = 10$ MeV remain unchanged.

Finally, the total collective factor is given by

$$K_{\text{coll}} = K_{\text{rot}}\phi(\beta_{20}) + K_{\text{vib}}[1 - \phi(\beta_{20})], \quad (18)$$

where $\phi(\beta_{20}) = [1 + \exp\{\frac{\beta_2^0 - \beta_{20}}{\Delta\beta_2}\}]^{-1}$ with $\beta_2^0 = 0.15$ and $\Delta\beta_2 = 0.04$ smoothly transitions the value of K_{coll} from large values of K_{rot} for saddle configurations to low values of K_{vib} for nearly spherical shapes, as introduced by Zagrebaev *et al.* [62].

Typical values of the spin-cutoff parameter σ_{\perp}^2 for rotational enhancement at the saddle point are in the range of 100–150, while the exponential factor in the vibrational enhancement for the ground state is around 10–15.

In addition to CELD, we will also consider the Kramers-Strutinsky factor K_{Kram} , which is commonly used in statistical model calculations. This factor multiplies the fission decay width, $K_{\text{Kram}}\Gamma_f$, reducing the probability of fission. Following the KEWPIE2 code [65], we assume that

$$K_{\text{Kram}} = \frac{\hbar\omega_{\text{gs}}}{T_{\text{gs}}} \left[\sqrt{1 + \left(\frac{\beta}{2\omega_{\text{sd}}}\right)^2} - \left(\frac{\beta}{2\omega_{\text{sd}}}\right) \right] \approx \frac{0.28 \text{ MeV}}{T_{\text{gs}}}. \quad (19)$$

In the above formula, $\hbar\omega_{\text{gs}} = \hbar\omega_{\text{sd}} = 1$ MeV, and the reduced friction parameter $\beta = 5 \text{ zs}^{-1}$.

In Fig. 17, we present calculations of the $\sum \sigma_{\alpha xn+2pyn} / \sum \sigma_{xn}$ ratio for the $^{210}\text{Ra}^*$ cascade: without attenuation of the fission barriers ($c_f = 1$), with CELD included, with both CELD and Kramers-Strutinsky factor included, and with lowered fission barriers ($c_f = 0.8$ for Ra isotopes with $A \leq 210$; see discussion in Sec. VC).

Only calculations with attenuated barriers can describe the data accurately. Inclusion of CELD alone shifts the initial calculations vertically and works like a constant scaling factor. The Kramers-Strutinsky factor works against CELD, and when both effects are considered, the final calculations are close to the initial case. A similar observation was made using

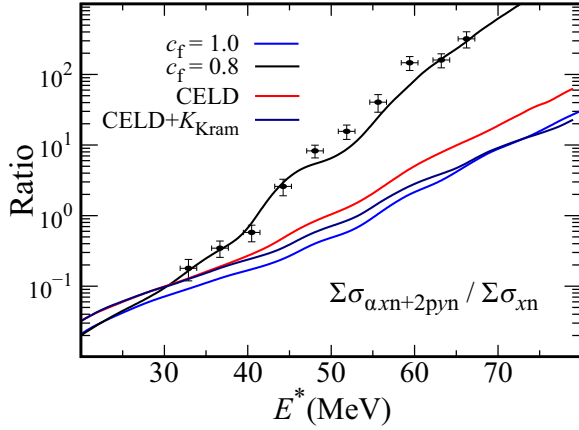


FIG. 17. Comparison of model calculations of the $\Sigma\sigma_{\alpha xn+2pyn} / \Sigma\sigma_{xn}$ ratio with different assumptions. Blue line: calculations without attenuation of the fission barriers ($c_f = 1$). Red line: calculations with CELD included. Navy line: calculations with both CELD and the Kramers-Strutinsky factor included. Black line: calculations with lowered fission barriers.

the KEWPIE2 code in Ref. [65]. Therefore, we conclude that CELD is not responsible for the enhancement of pxn and αxn channels.

F. Excitation Curves for $^{51}\text{V} + ^{159}\text{Tb}$

Finally, in Fig. 18 we present a comparison of model calculations with the experimental excitation curves for the $^{51}\text{V} + ^{159}\text{Tb}$ reaction. The obtained fusion probability $\langle P_{\text{fus}} \rangle = 0.02 \pm 0.01$, and is comparable to the value obtained for the $^{50}\text{Ti} + ^{159}\text{Tb}$ system. Calculations with this value of $\langle P_{\text{fus}} \rangle$ describe the data reasonably well at energies above the barrier for the $4n - 6n$, $p3n - p5n$, and $\alpha 3n - \alpha 4n$ channels. However, the calculations overestimate the cross sections for channels measured at below-barrier energies. This suggests that the fusion probability is lower in this energy region than assumed.

To estimate the fusion hindrance at energies below B_0 , in Fig. 19 we present the total measured ER cross section, $\Sigma\sigma_{\text{ER}}$, divided by the calculated total ER cross section with

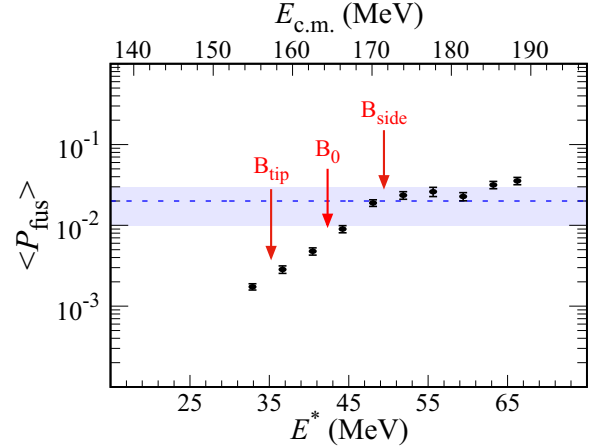


FIG. 19. Estimated $\langle P_{\text{fus}} \rangle$ as a function of energy. Arrows indicate the approximate tip-to-tip collision barrier, B_0 , and the side-collision barrier, respectively. The dashed line with an error corridor show the saturated value of $\langle P_{\text{fus}} \rangle = 0.02 \pm 0.01$.

$P_{\text{fus}} = 1$ assumed [see Eq. (10)]. Arrows indicate the approximate tip-to-tip collision barrier, B_0 , and the side-collision barrier, respectively. Although the estimated $\langle P_{\text{fus}} \rangle$ values are model dependent, we can expect a tenfold increase in fusion probability, from approximately 10^{-3} to 10^{-2} , when increasing the collision energy from below to above the barrier B_0 .

VI. CONCLUSION

The entrance-channel barrier distribution and excitation functions for various reaction channels were measured for the $^{51}\text{V} + ^{159}\text{Tb}$ system for the first time. The goal of the experiment was to assess the effect of nuclear deformation on the optimal reaction energy, particularly focusing on whether the side-collision configuration effect, previously observed in reactions of ^{48}Ca with actinides, is also present with lighter deformed targets. The analysis revealed that there might be approximately a tenfold difference, from 10^{-3} to 10^{-2} , in fusion probabilities between tip-to-tip and side collisions. The results support the hypothesis that nuclear deformation plays a

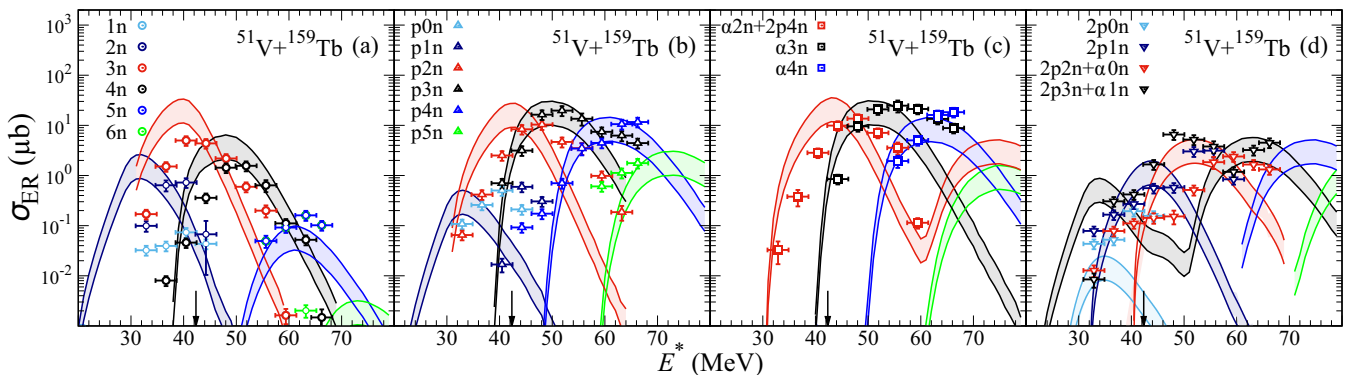


FIG. 18. Comparison of model calculations with experimentally measured cross sections for the $^{51}\text{V} + ^{159}\text{Tb}$ reaction. Error corridors correspond to values of $\langle P_{\text{fus}} \rangle$ ranging from 0.01 to 0.03. Vertical arrows indicate the excitation energies corresponding to collisions at $E_{\text{c.m.}} = B_0$.

critical role in determining the optimal beam energy for fusion reactions. However, the dependence of fusion probability on energy was obtained in a model-dependent manner and requires further investigation.

The increase in fusion probability correlates with the measured evaporation residue cross sections. The maximum for the xn evaporation channels was observed for the $3n$ channel at an energy close to the average entrance-channel barrier height, $B_0 = 164.5$ MeV. However, the highest cross section was observed for the $\alpha 3n$ channel at a higher energy, which aligns with the side-collision configuration, $B_{\text{side}} = 171.5$ MeV. The corresponding cross sections are $4.7 \pm 1.5 \mu\text{b}$ for $3n$ channel and $41.7 \pm 5 \mu\text{b}$ for $\alpha 3n$.

These measurements and observations are relatively well reproduced using standard statistical model calculations with fusion probabilities estimated based on experimental data. The model also reproduces the experimental data for ^{48}Ca and ^{50}Ti induced reaction on the same ^{159}Tb target. However, no enhancement of the αxn and pxn has been reported in these previous studies.

A comparison of these three reactions shows that the fusion probabilities for ^{50}Ti - and ^{51}V -induced reactions on a Tb target saturate at approximately the same level of 0.02 ± 0.01

at higher beam energies. This value is an order of magnitude smaller than that estimated for ^{48}Ca -induced reactions. Similar findings were obtained for cold fusion reactions with the same projectiles but with Pb and Bi targets. Whether such fusion probability behavior holds for new SHE synthesis reactions with beams heavier than ^{48}Ca is still an open question.

Further experiments and measurements using beams heavier than ^{48}Ca and other lanthanide targets may be needed to understand and confirm (or deny) the observed trend and discrepancies highlighted in this study. Furthermore, a more systematic approach to reactions on lanthanide targets with these beams could also provide more information on the lowering of the fission barriers and CELD effects in the studied mass region.

ACKNOWLEDGMENTS

One of the authors (T.C.) would like to express gratitude to Prof. Krystyna Siwek-Wilczyńska and Dr. Michał Kowal for valuable discussions and suggestions regarding the calculations. The calculations were performed at the Świerk Computing Centre (CIŚ) of the National Centre for Nuclear Research, Poland.

-
- [1] L. Öhrström and J. Reedijk, Names and symbols of the elements with atomic numbers 113, 115, 117 and 118 (IUPAC recommendations 2016), *Pure Appl. Chem.* **88**, 1225 (2016).
- [2] W. Myers and W. Swiatecki, Nuclear masses and deformations, *Nucl. Phys.* **81**, 1 (1966).
- [3] Y. Oganessian and V. Utyonkov, Super-heavy element research, *Rep. Prog. Phys.* **78**, 036301 (2015).
- [4] J. Roberto, C. Alexander, R. Boll, J. Burns, J. Ezold, L. Felker, S. Hogle, and K. Rykaczewski, Actinide targets for the synthesis of super-heavy elements, *Nucl. Phys. A* **944**, 99 (2015).
- [5] J. Khuyagbaatar *et al.*, Search for elements 119 and 120, *Phys. Rev. C* **102**, 064602 (2020).
- [6] S. Hofmann *et al.*, Review of even element super-heavy nuclei and search for element 120, *Eur. Phys. J. A* **52**, 180 (2016).
- [7] Y. Oganessian *et al.*, Attempt to produce element 120 in the $^{244}\text{Pu} + ^{58}\text{Fe}$ reaction, *Phys. Rev. C* **79**, 024603 (2009).
- [8] J. o. Gates, Towards the discovery of new elements: Production of livermorium ($Z = 116$) with ^{50}Ti , [arXiv:2407.16079](https://arxiv.org/abs/2407.16079).
- [9] I. Dragojević, K. Gregorich, C. Düllmann, M. Garcia, J. Gates, S. Nelson, L. Stavsetra, R. Sudowe, and H. Nitsche, Influence of projectile neutron number in the $^{208}\text{Pb}(^{48}\text{Ti}, n)^{255}\text{Rf}$ and $^{208}\text{Pb}(^{50}\text{Ti}, n)^{257}\text{Rf}$ reactions, *Phys. Rev. C* **78**, 024605 (2008).
- [10] J. Gates *et al.*, Comparison of reactions for the production of $^{258,257}\text{Db}$: $^{208}\text{Pb}(^{51}\text{V}, xn)$ and $^{209}\text{Bi}(^{50}\text{Ti}, xn)$, *Phys. Rev. C* **78**, 034604 (2008).
- [11] C. Folden III *et al.*, Measurement of the $^{208}\text{Pb}(\text{Cr}^{52}, n)\text{Sg}^{259}$ excitation function, *Phys. Rev. C* **79**, 027602 (2009).
- [12] S. L. Nelson, K. E. Gregorich, I. Dragojević, M. A. Garcia, J. M. Gates, R. Sudowe, and H. Nitsche, Lightest isotope of Bh produced via the $^{209}\text{Bi}(^{52}\text{Cr}, n)^{260}\text{Bh}$ reaction, *Phys. Rev. Lett.* **100**, 022501 (2008).
- [13] A. Lopez-Martens *et al.*, Measurement of proton-evaporation rates in fusion reactions leading to transfermium nuclei, *Phys. Lett. B* **795**, 271 (2019).
- [14] H. Sakai, H. Haba, K. Morimoto, and N. Sakamoto, Facility upgrade for superheavy-element research at RIKEN, *Eur. Phys. J. A* **58**, 238 (2022).
- [15] M. Tanaka *et al.*, Probing optimal reaction energy for synthesis of element 119 from $^{51}\text{V} + ^{248}\text{Cm}$ reaction with quasielastic barrier distribution measurement, *J. Phys. Soc. Jpn.* **91**, 084201 (2022).
- [16] T. Tanaka *et al.*, Study of quasielastic barrier distributions as a step towards the synthesis of superheavy elements with hot fusion reactions, *Phys. Rev. Lett.* **124**, 052502 (2020).
- [17] D. J. Hinde, M. Dasgupta, J. R. Leigh, J. P. Lestone, J. C. Mein, C. R. Morton, J. O. Newton, and H. Timmers, Fusion-fission versus quasifission: Effect of nuclear orientation, *Phys. Rev. Lett.* **74**, 1295 (1995).
- [18] T. Niwase, K. Fujita, Y. Yamano, K. Watanabe, D. Kaji, K. Morimoto, H. Haba, T. Hirano, S. Mitsuoka, and K. Morita, Measurement of fusion barrier distribution in $^{51}\text{V} + ^{208}\text{Pb}$ system, *JPS Conf. Proc.* **32**, 010022 (2020), Proceedings of 13th International Conference on Nucleus-Nucleus Collisions.
- [19] K. Hagino, N. Rowley, and A. Kruppa, A program for coupled-channel calculations with all order couplings for heavy-ion fusion reactions, *Comput. Phys. Commun.* **123**, 143 (1999).
- [20] D. Kaji, K. Morimoto, N. Sato, A. Yoneda, and K. Morita, Gas-filled recoil ion separator GARIS-II, *Nucl. Instrum. Methods Phys. Res., Sect. B* **317**, 311 (2013).
- [21] S. Kimura, D. Kaji, Y. Ito, H. Miyatake, K. Morimoto, P. Schury, and M. Wada, Reduction of contaminants originating from primary beam by improving the beam stoppers in GARIS-II, *Nucl. Instrum. Methods Phys. Res., Sect. A* **992**, 164996 (2021).
- [22] D. Kaji (private communication).

- [23] S. Ishizawa, K. Morimoto, D. Kaji, T. Tanaka, and F. Tokanai, Improvement of the detection efficiency of a time-of-flight detector for superheavy element search, *Nucl. Instrum. Methods Phys. Res., Sect. A* **960**, 163614 (2020).
- [24] P. Brionnet, R. Grzywacz, D. Kaji, T. King, T. Niwase, K. Morimoto, K. Rykaczewski, and H. Sakai, Development of digital electronics for the search of she nuclei using GARIS-II/III at RIKEN, *Nucl. Instrum. Methods Phys. Res., Sect. A* **1049**, 168068 (2023).
- [25] R. Akyuz and A. Winther, Parameterization of the nucleus-nucleus potential, in *Nuclear Structure and Heavy-ion Reactions, Proceedings of the International School of Physics E. Fermi* (North-Holland, Amsterdam, 1981), p. 491.
- [26] B. Pritychenko, M. Birch, B. Singh, and M. Horoi, Tables of $E2$ transition probabilities from the first 2^+ states in even-even nuclei, *At. Data Nucl. Data Tables* **107**, 1 (2016).
- [27] P. Möller, A. Sierk, T. Ichikawa, and H. Sagawa, Nuclear ground-state masses and deformations: FRDM (2012), *At. Data Nucl. Data Tables* **109-110**, 1 (2016).
- [28] C. Bland, Choosing fitting functions to describe peak tails in alpha-particle spectrometry, *Appl. Radiat. Isot.* **49**, 1225 (1998).
- [29] National Nuclear Data Center, Brookhaven National Laboratory, NUDAT (Nuclear Structure and Decay Data, 2008).
- [30] K. Gregorich *et al.*, Attempt to confirm superheavy element production in the $^{48}\text{Ca} + ^{238}\text{U}$ reaction, *Phys. Rev. C* **72**, 014605 (2005).
- [31] W. Parker *et al.*, Charged-particle evaporation from hot composite nuclei: Evidence over a broad Z range for distortions from cold nuclear profiles, *Phys. Rev. C* **44**, 774 (1991).
- [32] K. Hagino, Hot fusion reactions with deformed nuclei for synthesis of superheavy nuclei: An extension of the fusion-by-diffusion model, *Phys. Rev. C* **98**, 014607 (2018).
- [33] D. A. Mayorov, T. A. Werke, M. C. Alfonso, E. E. Tereshatov, M. E. Bennett, and C. M. Folden III, Production cross sections of elements near the $N = 126$ shell in ^{48}Ho -induced reactions with ^{154}Gd , ^{159}Tb , ^{162}Dy , and ^{165}Ho targets, *Phys. Rev. C* **90**, 024602 (2014).
- [34] D. A. Mayorov, T. A. Werke, M. C. Alfonso, E. E. Tereshatov, M. E. Bennett, M. M. Frey, and C. M. Folden III, Evaporation residue excitation function measurements in ^{50}Ti - and ^{54}Cr -induced reactions with lanthanide targets, *Phys. Rev. C* **92**, 054601 (2015).
- [35] K. Siwek-Wilczyńska and J. Wilczyński, Empirical nucleus-nucleus potential deduced from fusion excitation functions, *Phys. Rev. C* **69**, 024611 (2004).
- [36] X. Bao, Fusion dynamics of low-energy heavy-ion collisions for production of superheavy nuclei, *Front. Phys.* **8**, 14 (2020).
- [37] E. Chernysheva *et al.*, Cross sections of the production of mercury and radon isotopes in complete fusion reactions with $^{36,40}\text{Ar}$ and $^{40,48}\text{Ca}$ projectiles, *Bull. Russ. Acad. Sci. Phys.* **86**, 883 (2022).
- [38] D. Hinde and M. Dasgupta, Insights into the dynamics of fusion forming heavy elements, *Nucl. Phys. A* **787**, 176 (2007).
- [39] T. A. Werke, D. A. Mayorov, M. C. Alfonso, E. E. Tereshatov, and C. M. Folden III, Hot fusion-evaporation cross sections of ^{44}Ca -induced reactions with lanthanide targets, *Phys. Rev. C* **92**, 054617 (2015).
- [40] T. Cap, K. Siwek-Wilczyńska, and J. Wilczyński, Nucleus-nucleus cold fusion reactions analyzed with the l -dependent “fusion by diffusion” model, *Phys. Rev. C* **83**, 054602 (2011).
- [41] D. Hinde, M. Dasgupta, and E. Simpson, Experimental studies of the competition between fusion and quasifission in the formation of heavy and superheavy nuclei, *Prog. Part. Nucl. Phys.* **118**, 103856 (2021).
- [42] A. Berriman, D. Hinde, M. Dasgupta, C. Morton, R. Butt, and J. Newton, Unexpected inhibition of fusion in nucleus–nucleus collisions, *Nature (London)* **413**, 144 (2001).
- [43] R. Sagaidak *et al.*, Fusion suppression in mass-asymmetric reactions leading to Ra compound nuclei, *Phys. Rev. C* **68**, 014603 (2003).
- [44] W. Reisdorf, Analysis of fissionability data at high excitation energies: I. The level density problem, *Z. Phys. A* **300**, 227 (1981).
- [45] A. Ignatyuk, G. Smirenkin, and A. Tishin, Phenomenological description of energy dependence of the level density parameter, *Yad. Fiz.* **21**, 485 (1975).
- [46] K. Siwek-Wilczyńska, T. Cap, and M. Kowal, Exploring the production of new superheavy nuclei with proton and α -particle evaporation channels, *Phys. Rev. C* **99**, 054603 (2019).
- [47] W. Huang, M. Wang, F. Kondev, G. Audi, and S. Naimi, The ame 2020 atomic mass evaluation (I). Evaluation of input data, and adjustment procedures, *Chin. Phys. C* **45**, 030002 (2021).
- [48] M. Wang, W. Huang, F. Kondev, G. Audi, and S. Naimi, The AME 2020 atomic mass evaluation (II). Tables, graphs and references, *Chin. Phys. C* **45**, 030003 (2021).
- [49] P. Möller, A. Sierk, T. Ichikawa, A. Iwamoto, R. Bengtsson, H. Uhrenholt, and S. Åberg, Heavy-element fission barriers, *Phys. Rev. C* **79**, 064304 (2009).
- [50] P. Jachimowicz, M. Kowal, and J. Skalski, Properties of heaviest nuclei with $98 \leq Z \leq 126$ and $134 \leq N \leq 192$, *At. Data Nucl. Data Tables* **138**, 101393 (2021).
- [51] A. Yeremin, Regularities of formation and survival probability of compound nuclei in the region of $Z \geq 82$: Study of complete-fusion reactions with heavy ions using the kinematic separator VASSILISSA, *Phys. Part. Nuclei* **38**, 492 (2007).
- [52] S. Baba *et al.*, Evaporation residue formation competing with the fission process in the $^{197}\text{Au} + ^{16}\text{O}$, ^{12}C reactions and fission barriers at a specifiedj window, *Z. Physik A* **331**, 53 (1988).
- [53] K. Mahata, S. Kailas, A. Shrivastava, A. Chatterjee, A. Navin, P. Singh, S. Santra, and B. Tomar, Fusion of ^{19}F with $^{188,192}\text{Os}$, *Nucl. Phys. A* **720**, 209 (2003).
- [54] A. Shrivastava, S. Kailas, A. Chatterjee, A. M. Samant, A. Navin, P. Singh, and B. S. Tomar, Shell effects in fission fragment anisotropies for $^{12}\text{C} + ^{194,198}\text{Pt}$ systems, *Phys. Rev. Lett.* **82**, 699 (1999).
- [55] E. Prasad *et al.*, Evaporation residue excitation function measurement for the $^{16}\text{O} + ^{194}\text{Pt}$ reaction, *Phys. Rev. C* **84**, 064606 (2011).
- [56] L. Corradi *et al.*, Excitation functions for $^{208-211}\text{Fr}$ produced in the $^{18}\text{O} + ^{197}\text{Au}$ fusion reaction, *Phys. Rev. C* **71**, 014609 (2005).
- [57] T. Banerjee, S. Nath, and S. Pal, Fusion probability in heavy nuclei, *Phys. Rev. C* **91**, 034619 (2015).
- [58] W. Loveland, An experimentalist’s view of the uncertainties in understanding heavy element synthesis, *Eur. Phys. J. A* **51**, 120 (2015).
- [59] A. Andreyev *et al.*, Decay widths of highly excited Ra compound nuclei, *Nucl. Phys. A* **620**, 229 (1997).
- [60] D. Vermeulen, H. Clerc, C. Sahn, K. Schmidt, J. Keller, G. Münzenberg, and W. Reisdorf, Cross sections for evaporation

- residue production near the $N = 126$ shell closure, *Z. Phys. A* **318**, 157 (1984).
- [61] J. R. Grover and J. Gilat, Emission of alpha particles from nuclei having large angular momenta, *Phys. Rev.* **157**, 823 (1967).
- [62] V. I. Zagrebaev, Y. Aritomo, M. G. Itkis, Y. T. Oganessian, and M. Ohta, Synthesis of superheavy nuclei: How accurately can we describe it and calculate the cross sections? *Phys. Rev. C* **65**, 014607 (2001).
- [63] A. Karpov, A. Denikin, M. Naumenko, A. Alekseev, V. Rachkov, V. Samarin, V. Saiko, and V. Zagrebaev, NRV web knowledge base on low-energy nuclear physics, *Nucl. Instrum. Methods Phys. Res., Sect. A* **859**, 112 (2017).
- [64] A. Junghans, M. De Jong, H. Clerc, A. Ignatyuk, G. Kudyaev, and K. Schmidt, Projectile-fragment yields as a probe for the collective enhancement in the nuclear level density, *Nucl. Phys. A* **629**, 635 (1998).
- [65] H. Lü, A. Marchix, Y. Abe, and D. Boilley, KEW-PIE2: A cascade code for the study of dynamical decay of excited nuclei, *Comput. Phys. Commun.* **200**, 381 (2016).
- [66] S. Komarov, R. Charity, C. Chiara, W. Reviol, D. Sarantites, L. Sobotka, A. Caraley, M. Carpenter, and D. Seweryniak, Search for the fade out of a collective enhancement of the nuclear level density, *Phys. Rev. C* **75**, 064611 (2007).
- [67] R. N. Sagaidak and A. N. Andreyev, Fission barriers for Po nuclei produced in complete fusion reactions with heavy ions, *Phys. Rev. C* **79**, 054613 (2009).